High-Power Test of Two Prototype X-band Accelerating Structures Based on SwissFEL Fabrication Technology

William L. Millar, Alexej Grudiev, Walter Wuensch, Nuria Catalán Lasheras, Gerard McMonagle, Riccardo Zennaro, Paolo Craievich, Markus Bopp, Thomas G. Lucas, Matteo Volpi, Jan Paszkiewicz, Amelia Edwards, Rolf Wegner, Hikmet Bursali, Benjamin Woolley, Anastasiya Magazinik, Igor Syratchev, Anna Vnuchenko, Samantha Pitman, Verónica del Pozo Romano, David Bañón Caballero, and Graeme Burt

***Abstract*—This paper presents the design, construction, and high-power test of two X-band radio-frequency (RF) accelerating structures built as part of a collaboration between CERN and the Paul Scherrer Institute (PSI) for the Compact Linear Collider (CLIC) study. The structures are a modified "tuning-free" variant of an existing CERN design and were assembled using Swiss Free Electron Laser (SwissFEL) production methods. The purpose of the study is twofold; the first objective is to validate the RF properties and high-power performance of the tuning-free, vacuum brazed PSI technology. The second objective is to study the structures' high-gradient behaviour to provide insight into the breakdown and conditioning phenomena as they apply to high-field devices in general. Low-power RF measurements showed that the structure field profiles were close to the design values, and both structures were conditioned to accelerating gradients in excess of 100 MV/m in CERN's high-gradient test facility. Measurements performed during the second structure test suggest that the BDR scales strongly with the accelerating gradient, with the best fit being a power law relation with an exponent of 31.14. In both cases, the test results indicate that stable, high-gradient operation is possible with tuning-free, vacuum brazed structures of this kind.**

***Index Terms*—Acceleration, Breakdown, High-Gradient, LINAC, Radio frequency, Test Facilities, Vacuum Arc, X-band.**

I. Introduction

THE CLIC collaboration has invested significant effort in the development of high-gradient normal conducting linear accelerator cavities (LINACs). One of the key feasibility issues of the study is the demonstration of an unloaded accelerating gradient of 100 MV/m at a pulse length of 240 ns and a breakdown rate (BDR) 3×10^{-7} breakdowns/pulse/metre (bpp/m) in the accelerating structures for the main LINAC [1].

William L. Millar (e-mail: lee.millar@cern.ch), Alexej Grudiev, Walter Wuensch, Nuria Catalán Lasheras, Gerard McMonagle, Matteo Volpi, Jan Paszkiewicz, Amelia Edwards, Rolf Wegner, Hikmet Bursali, Benjamin Woolley, Anastasiya Magazinik, Igor Syratchev, Samantha Pitman, Anna Vnuchenko, Verónica del Pozo Romano, and David Bañón Caballero are with CERN, 1211 Geneva, Switzerland.

Riccardo Zennaro, Paolo Craievich, Thomas G. Lucas, and Markus Bopp are with the Paul Scherrer Institute, 5232 Villigen, Switzerland.

Graeme Burt is with the Cockcroft Institute, Lancaster University, Lancaster LA1 4YW, United Kingdom.

David Bañón Caballero is also with the Instituto de Física Corpuscular (IFIC) (CSIC-Univ. Valencia), 46980 Paterna, Valencia, Spain.

Hikmet Bursali is also with the department of Basic and Applied Sciences for Engineering (SBAI), Sapienza University of Rome, 00161 Rome, Italy.

Matteo Volpi is also with the University of Melbourne, Parkville VIC 3010, Australia.

To date, over twenty prototype X-band (12 GHz) accelerating structures have reached unloaded accelerating gradients of 100 MV/m during testing [2–5] and recently, high-gradient X-band technology has also found use in other applications including free electron lasers (FELs) [6, 7], radiation therapy [8, 9], and inverse Compton scattering (ICS) sources [10]. Typically, individual precision machined disks are stacked and diffusion bonded to form the multi-cell accelerating sections on the CLIC structures [11]. However, to compensate for dimensional errors, tuning is often required. Generally, this is accomplished by manually pushing or pulling on small pins which are brazed to the cell exteriors and [12], due to its iterative nature, the process can be time-consuming, particularly in multi-structure arrangements.

To avoid the need for tuning after structure fabrication, a high-precision manufacturing process has been developed at the Paul Scherrer Institute [13]. The SwissFEL project requires 120 C-band accelerating structures operating at a nominal gradient of 28.5 MV/m [14]. The structures designed for the facility are vacuum brazed and boast a "tuning free" cell design, with the required tolerances instead being met via machining and assembly alone. However, the average resonant frequency or average phase advance per cell may still be adjusted by varying the cavity temperature [15]. During high-power tests, a prototype C-band structure of this kind established an accelerating gradient in excess of 50 MV/m, and so the manufacturing method is also of interest in the context of high-gradient structure development [16].

For this reason, two X-band T24 CLIC prototype structures have been manufactured using the PSI SwissFEL production methods, referred to as the T24 PSI N1 and T24 PSI N2 respectively. To date, the T24 cavity is one of the most well tested designs for CLIC [4, 17–21], making it well suited to a comparative study with a tuning-free, vacuum brazed variant. The results of the first structure test have been partially reported previously [22, 23], however both tests are presented in their entirety in this paper to provide a more comprehensive overview of the design performance.

II. Radio Frequency Design

The structure is comprised of 24 regular accelerating cells with a tapering of the iris radius from 3.15 mm to 2.35 mm

in the downstream direction. The iris tapering results in a reduction in the group velocity from 1.8 to 0.9%c and provides constant distribution of the loaded accelerating gradient along the structure. To compensate for the change in RF frequency caused by this tapering, the external diameter of each cell decreases from 21.96 to 20.69 mm. Notably, the cells are azimuthally symmetric and thus, do not have the wakefield damping present in the CLIC baseline design [1]. Couplers of the mode launcher type convert the TE_{10} waveguide mode to the TM_{010} cavity operating mode [24]. Each coupler is comprised of a cylindrical section with dual waveguide feeds and an additional cell to match the low impedance of circular waveguide section to the high impedance of the central, regular accelerating cells. A cross section of the structure is shown in Fig. 1.

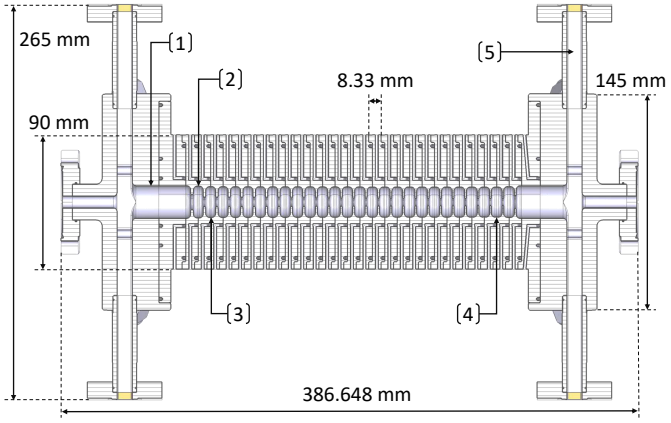

Fig. 1: Longitudinal cross section of a 3D model of the T24 PSI accelerating structure showing the mode launcher section (1), the input matching cell (2), the first (3) and final (4) regular accelerating cells, and one of the waveguide outputs (5). Several key dimensions are also included.

To operate at an average unloaded gradient of 100 MV/m over the 24 regular cells, an input power of 37.5 MW is required. At this power, the peak surface electric and magnetic fields established within the structure are approximately 210 MV/m and 260 kA/m respectively. Previously, a quantity referred to as the modified Poynting vector (S_c) was also proposed as a potential high-gradient performance limit in accelerating structures due to RF breakdown [25]. It has been reported that to reach a BDR below 1×10^{-6} bpp/m at a pulse length of 200 ns, this value should not exceed 5 MW/mm^2. In the T24 PSI structure, an input power of 37.5 MW corresponds to a peak modified Poynting vector of 3.8 MW/mm^2. Several key cavity parameters are summarised in Table I.

III. Mechanical Design, Fabrication, and Assembly

Mechanically, the structures are similar to the SwissFEL C-band structures, being comprised of precision machined copper disks [15]. Both sides of the disks are machined, leaving the brazing plane in the centre of the cells, unlike the CLIC baseline structures in which the cell features are machined on one side only, leaving the other flat [1]. Cooling channels are integrated into the disk perimeters, running longitudinally along the structure with inlets situated on the coupling cells. A rendering of a constituent disk is shown in Fig. 2.

TABLE I: Summary of key cavity parameters. The electromagnetic values quoted correspond to operation with an unloaded accelerating gradient of 100 MV/m across the regular accelerating cells only, not the couplers.

Parameter	Value
Frequency (MHz)	11994.2
No. of accelerating cells	24+2 couplers
Phase advance per cell (°)	120
Cell diameter (mm)	21.96 - 20.69
Iris aperture diameter (mm)	6.30 - 4.70
Iris thickness (mm)	1.67 - 1.00
v_g (%c)	1.8 - 0.912
t_{fill} (ns)	59
Q_0	7475
P_{in} for 100 MV/m unloaded (MW)	37.5
E_{Surf} @ 100 MV/m unloaded (MV/m)	210
H_{Surf} @ 100 MV/m unloaded (kA/m)	260
S_c @ 100 MV/m unloaded (MW/mm^2)	3.8

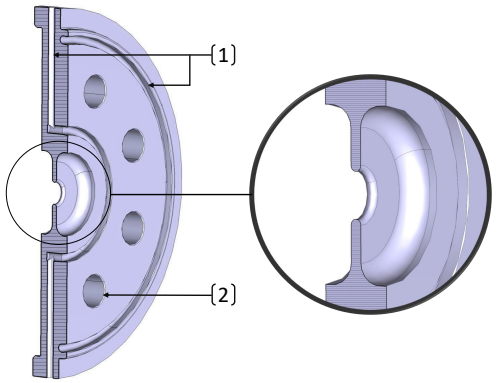

Fig. 2: Cross-section of a rendering of a constituent disk showing the channels for the brazing alloy (1) and the integrated cooling channels (2). One half of an RF cell is present on each side of the central portion of disk (shown in the close-up).

The disks were machined by VDL Enabling Technologies Group [26], and all their profiles were all within the specified $\pm$ 2 μm tolerance while the average surface roughness (Ra) was less than 20 nm. To remove surface contaminants, the disks were then baked at 400°C for two hours prior to brazing. Due to the reduced overall disk diameter, use of the KUKA KR 30 HA robotic arm which is typically employed during the assembly of the C-band SwissFEL structures was not possible, and so the disks were stacked manually prior to brazing [13, 27]. After brazing, the final straightness was within 10 μm. A CAD rendering of the full structure assembly is showing in Fig. 3.

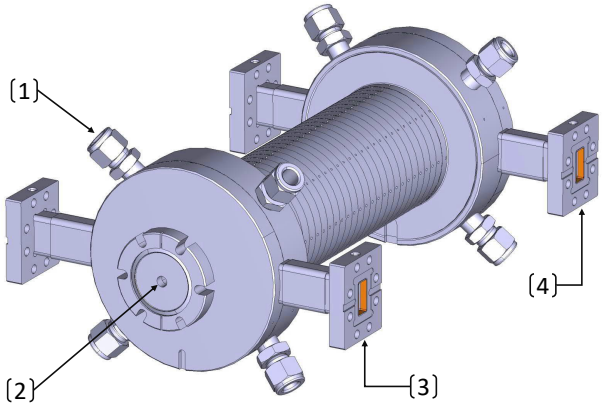

Fig. 3: Isometric view of a rendering of the full structure assembly with labels showing one of the cooling water inlets (1), the beam pipe entry (2), and the waveguide input (3) and outputs one one side (4).

IV. Low-Power Measurement

Prior to the high-power tests, S-parameter and bead pull measurements of both structures were performed at CERN. In the latter, a small dielectric bead is moved through the structure on the beam line axis while the structure S-parameters are monitored. The insertion of the bead constitutes a local impedance mismatch, resulting in a small reflection. In travelling wave accelerating structures, the change in the complex reflection associated with the bead when on-axis is proportional to the square of the complex electric field. Hence, its amplitude and phase may be calculated by taking the square root of this value. Further details of the methodology are reported elsewhere [28].

During the measurements, each structure was mounted in an upright position as shown in Fig. 4. To perform the bead pull, a nylon wire was then lowered into the structure vertically and used, in conjunction with a pulley system, to slowly guide the bead along the central axis while avoiding contact with the irises. To compensate for the frequency shift associated with the introduction of the wire, the S-parameters were logged both prior to, and after, its insertion. The insertion of the wire resulted in frequency shifts of -0.55 and -0.52 MHz in the first and second structures respectively.

During RF measurements, changes in the ambient temperature result in thermal expansion or contraction of the cavity. The relative frequency change associated with this effect is, in the first-order approximation, proportional to the linear strain. As such, the temperature was controlled, monitored, and recorded during the measurements. The cavity frequency also scales inversely with the square root of the relative permittivity, ϵ_r, of the measurement medium. As the wire for the bead pull must be passed through the structure, conducting the measurements in vacuum is generally not feasible, and so the cavity was instead held under dry nitrogen flow. Although it is possible to carry out the procedure in air, the relative permittivity is, in part, determined by the relative humidity [29], and so additional measurements are necessary to avoid the introduction of error.

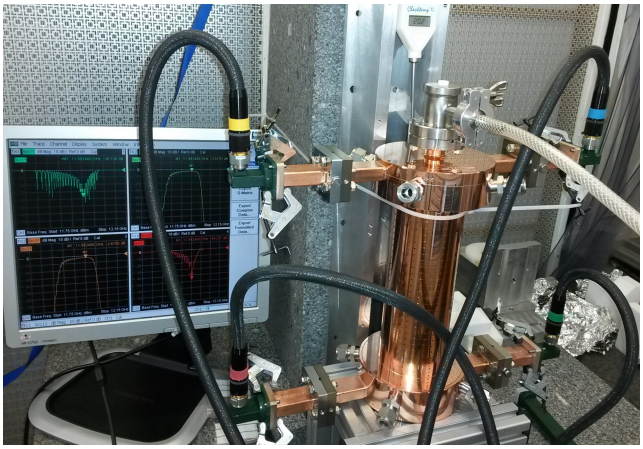

Fig. 4: The T24 PSI N2 during the low-power RF measurement. A nitrogen inlet is visible on top of the structure.

At the equivalent operating frequency under vacuum, reflections of -31 dB and -36 dB were achieved in the T24 PSI N1 and T24 PSI N2 respectively, while the average phase advance per cell was $120° \pm 1.6°$ (std). In Fig. 5 (c), the peaks corresponding to the accelerating cells are positioned further right than those in (d), indicating that the bead was likely situated further from the structure input when commencing the measurement of the PSI T24 N1. A periodic variation in the field amplitude is visible in both structures, indicating the presence of a small standing wave component. It is speculated that this may be due to a mismatch of the last two cells, however the overall profiles are as expected, indicating that all the cells were very well machined and assembled.

In Figs. 5 (c) and (d), some field is also seen before and after the peaks associated with the matching and regular accelerating cells. These regions correspond to the cylindrical waveguide section of the mode launcher. In this section, the E-field is smaller than in the regular accelerating cells, meaning the relative error in the measurement is larger. Notably, in Fig. 5 (c) the field measured in the mode launcher is longer than in (d). This can be attributed to slippage in the pulley system used to maintain tension in the wire, or to an adjustment being made to the setup early in the measurement. However, as the primary objective is to ensure that the field distribution and phase advance in the accelerating cells are acceptable, the discrepancy in this region is viewed as unimportant.

V. Experimental Setup

Following the low-power RF measurements, both structures were tested at CERN. To date, CERN has commissioned three X-band klystron-based test stands named Xbox-1, Xbox-2, and Xbox-3 respectively [30, 31]. As none of the work presented in this paper was performed in the Xbox-1 test stand, particular attention will be paid to the latter two. A diagram of the high-power portion of the Xbox-2 test stand is shown in Fig. 6.

In each of the test stands, directional couplers are used to sample the RF signals throughout the waveguide network and Faraday cups are used to measure the charge which is emitted via field emission, or during breakdowns. Threshold detectors

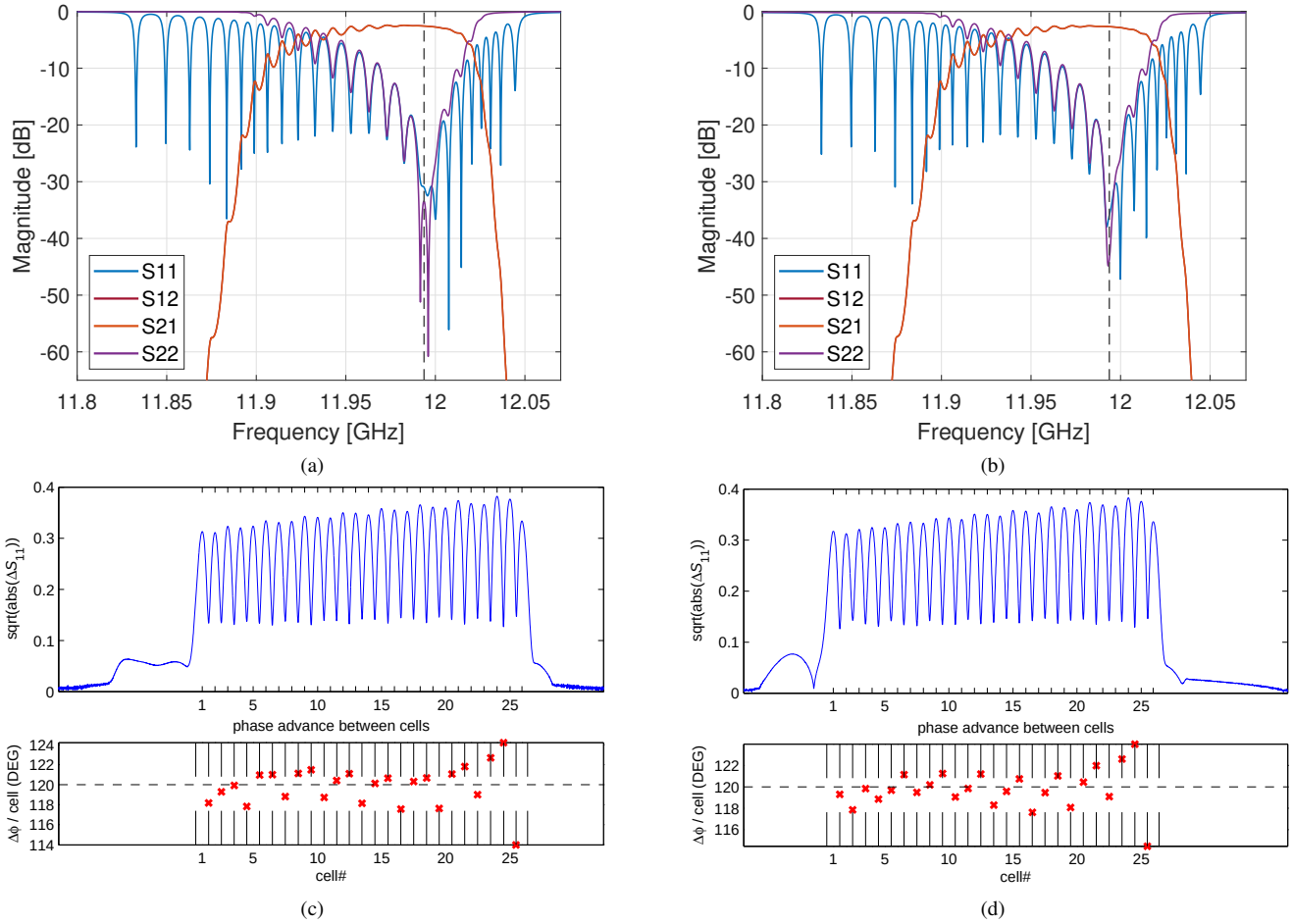

Fig. 5: S-parameters of the T24 PSI N1 (a) and T24 PSI N2 (b). The equivalent operating frequencies at 35.5° and 36° under vacuum are shown by the black dashed lines, where reflections of -31 dB and -36 dB were recorded respectively. The electric field profiles on the beam line axis (top) and the phase advance per cell (bottom) measured during the bead pull of the T24 PSI N1 (c) and T24 PSI N2 (d) structures are also shown. In the bead pull measurements the structure input is on the left side.

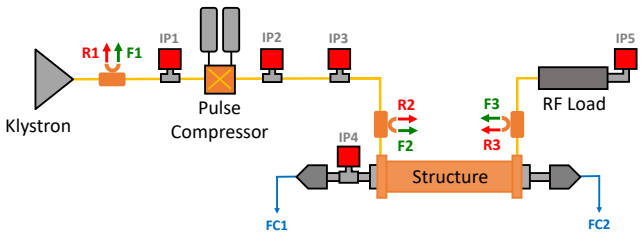

Fig. 6: A diagram of CERN's Xbox-2 test stand. The red and green arrows show where the forward (F) and reflected (R) RF signals are measured via directional couplers, while the upstream and downstream Faraday cup signals are labelled FC1 and FC2 respectively. The locations of the ion pumps (IP) throughout the system are also shown.

on the reflected RF signals and the Faraday cup signals are then used to detect RF breakdowns during operation. Generally, breakdowns act as a short circuit and reflect the incoming RF power back towards the source. Hence, the RF signals may be used to determine the location of the breakdown. For example, if a breakdown occurs in the structure, the threshold detection on signals R2 and possibly R1 in Fig. 6 will be activated, while signal F3 will be truncated. Each test stand is also equipped additional auxiliary temperature and pressure sensors throughout the waveguide network.

While Xbox-2 has a single klystron and test slot, Xbox-3 has four. Each pair of test slots in Xbox-3 utilises a scheme in which a pair of 6 MW Toshiba klystrons are combined via a 3 dB hybrid and sent to a pulse compressor to produce the high-power RF pulse which is delivered to the device under test (DUT). The use of the hybrid means that by appropriately adjusting the phase of klystron pulses, the RF power can be directed to either test slot. The relatively low power of the klystrons also means that operation is possible at pulse repetition rates of up to 400 Hz. This allows the use of different repetition rates to be investigated, and generally increases the structure throughput in the test stand. Conversely, the 50 MW klystron in use in Xbox-2 is limited to a pulse repetition rate of 50 Hz, and the RF pulse is fed directly into a pulse compressor. Further details on each scheme have been reported elsewhere [23, 30–32], however the key specifications for the

Xbox-2 and Xbox-3 test stands are summarised in Table II.

TABLE II: Key parameters for two of CERN's High-Gradient Test Stands. For compressed pulse lengths of 50-250 ns, peak power gains in the range of 3-4 are typical.

Parameter	**Xbox-2**	**Xbox-3**	**Unit**
Frequency	11994.2	11994.2	MHz
No. Test Slots	1	4	–
Klystron			
Model	XL-5 [33–35]	E37113 (×4) [36–38]	–
Peak Power	50	6	MW
Pulse Length	$\leq$1.5	$\leq$5	μs
Repetition Rate	$\leq$50	$\leq$400	Hz
Pulse Comp.			
Type	SLED-I [39, 40]	SLED-I (×4)	–
Q_0	180,000	180,000	–
Q_{ext}	30,000	40,000	–

Although the intrinsic quality factor, Q_0, of the pulse compressor cavities in each test stand was made as high as possible, the external quality factors Q_{ext} were chosen such that the cavities can be filled to their maximum stored energy within the RF pulse available from the klystron [40]. Consequently, the compressed pulses delivered to the DUT by each test stand generally differ in shape. An example is shown in Fig. 7.

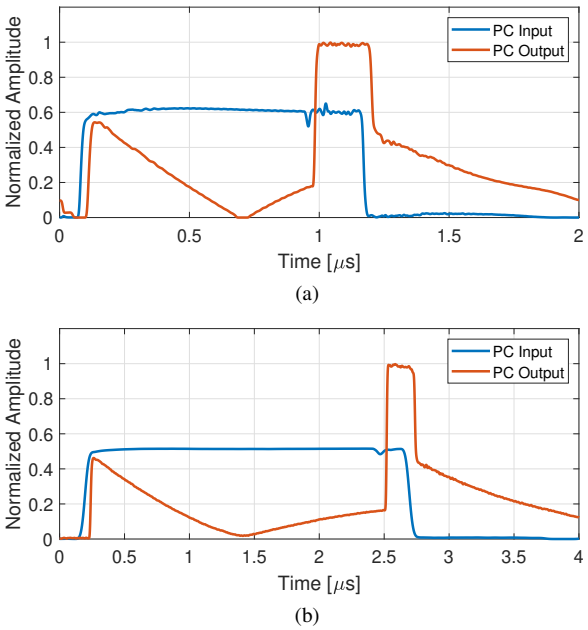

Fig. 7: The normalized amplitude envelopes of the RF pulses sent to the pulse compressor (PC Input) and compressed pulses delivered to the DUT (PC Output) in Xbox-2 (a) and Xbox-3 (b) respectively. Two klystron pulses have been combined to form the PC input signal in the Xbox-3 example. In each case, the rectangular klytron pulse has been compressed to provide a 200 ns compressed pulse.

VI. High-Power Test of the First Structure

Initially, the T24 PSI N1 was installed the Xbox-3 test slot, before being moved to Xbox-2 for the second portion of the test period. Preliminary structure conditioning was performed using an algorithm which was developed in-house at CERN. In summary, the control system maintains an operator selected BDR by increasing the structure input power in 10 kW steps at regular intervals. When the target gradient is reached, the system then ceases ramping. A more detailed description of the algorithm is available elsewhere [30]. As the purpose of the algorithm is to protect the entire system, breakdowns which occur anywhere in the high-power waveguide network (i.e. in the pulse compressors or RF loads) are also counted in the calculation of the BDR. Generally, breakdowns are accompanied by an increase in pressure in the waveguide network, and if one is detected, RF pulsing is inhibited for several seconds. Depending on the system BDR, and the control system settings, the occurrence of a breakdown can also result in the operating power being reduced, usually by several kW.

Following breakdowns, the power is then slowly ramped back up to the pre-breakdown level, minus any reduction which has been implemented. As the power level is regulated by a proportional–integral–derivative (PID) controller, the speed at which the field is re-established following breakdowns is determined by the PID gains and to prevent overshoot, the controller is typically tuned to return to full power in approximately 1000 pulses. An example of the post-breakdown ramping procedure, and the corresponding pressure reading, is shown in Fig. 8.

The full conditioning history of the T24 PSI N1 is presented in Fig. 9. The gradient and pulse lengths shown were calculated from the RF waveforms which were logged during operation, after being calibrated to provide a reading in power. The gradient was taken as the average value of the flat top of the compressed pulse, while the pulse length was taken as the full width at half maximum (FWHM). In the test stands, the RF signals are down-mixed from 12 GHz to 400 MHz, and then sampled at 1.6 GS/s by an NI-5772 digitizer. An in-phase and quadrature (I/Q) demodulation scheme is used to recover the amplitude and phase of the corresponding 12 GHz RF signal. A standard quadratic function is used to obtain a power reading, and so the FWHM of the calibrated waveform would correspond to the full width at $\approx$70% of the maximum of the amplitude envelopes shown in Fig. 7. Further details of the acquisition system and calibration procedure are available elsewhere [30, 31].

Pulsing in CERN's Xbox-3 test slot commenced in March 2017 and the structure was algorithmically conditioned up to an unloaded gradient of 100 MV/m at a pulse length of 70 ns with a BDR set point of 5×10^{-5} bpp (breakdowns per pulse). After 150 million pulses, the pulse length was increased to 150 ns and the operating gradient was reduced by 15% to maintain an approximately constant BDR. To ensure that the chillers could still effectively regulate the pulse compressor temperature, the repetition rate was also reduced to 50 Hz. The structure was then ramped back up to an unloaded gradient

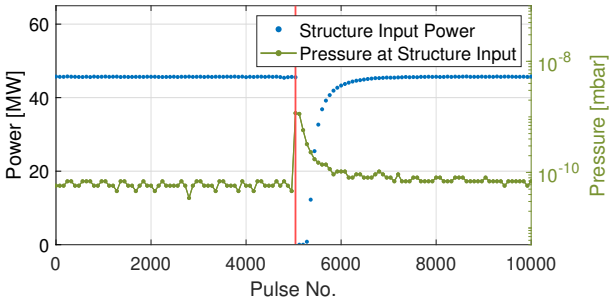

Fig. 8: A typical post-breakdown recovery process showing the pressure measured by the ion pump situated at the structure input (green) and the DUT input power (blue). The pulse on which the breakdown occurred is indicated by the red line.

of 100 MV/m. After approximately 250 million total pulses, a klystron problem necessitated a reduction in the operating power, and so the structure was held at lower gradients until the 420 million pulse mark.

After replacing the klystron, the structure was gradually conditioned up to an operating gradient of 107 MV/m at 100 ns. After approximately 715 million pulses, the pulse length was increased to 200 ns, however the compression ratio and available RF power limited operation to a gradient of 93 MV/m. Due to these power limitations, the structure was removed from Xbox-3 and installed in Xbox-2 to be tested at higher power. Prior to disassembly, the waveguide network was slowly filled with nitrogen until atmospheric pressure was reached. The structure was then removed and the waveguide manifolds were covered with aluminium foil, with the cavity surface being exposed to air in the process. Generally, structures are sealed in nitrogen filled enclosures and placed into storage after testing. However, given that the plan was to continue the test in Xbox-2, and that Xbox-2 and Xbox-3 high-power test slots are located in a common bunker, the structure was moved to the Xbox-3 test slot immediately for installation. The Xbox-3 waveguide network assembly process was completed the following morning, and so, although the structure manifolds were covered, the cavity surface was exposed to air at atmospheric pressure for a total of approximately 30 hours before being pumped down. The effect of this exposure is examined later in Section VIII.

The test period in Xbox-2 commenced in October 2017 and the structure was ramped up to an unloaded gradient of 103 MV/m over the course of approximately 60 million pulses. After a short period operating at fixed input power, ramping continued until gradients which had not previously been attained in Xbox-3 were reached. After reaching an unloaded gradient of 115 MV/m, the pulse length was increased to 100 ns and the gradient was reduced to maintain an approximately constant BDR. Ramping then resumed and the process was repeated, with the structure ultimately reaching a gradient of 115 MV/m at a pulse length of 210 ns after 250 million pulses. While operating at this gradient and pulse length, the BDR did not reduce as expected, and reached values on the order of 1×10^{-4} bpp. For this reason, the gradient was then reduced to 105 MV/m after 400 million pulses. Upon doing so, the BDR dropped immediately by an order of magnitude, however it was decided that the high-power limit of the structure had likely been reached, and that some damage accrued during the test may have prevented conditioning to lower BDRs.

A. *Spatial Distribution of Breakdowns*

As stated in Section V, breakdowns generally behave like a short circuit, reflecting the incoming RF power. The longitudinal position of the structure breakdowns can, therefore, be inferred by calculating the difference in time between the rising and falling edges of the reflected and transmitted signals reaching the directional couplers at the structure input and output respectively [23, 41, 42]. The breakdown distribution was examined regularly throughout the test to track the conditioning progress of the structure and to monitor for the emergence of so-called "hot" cells, which have an elevated local BDR, and could be indicative of damage, a defect, or contamination. The results for the test periods in both the Xbox-3 and Xbox-2 test stands are shown separately in Fig. 10.

During the first 200 million pulses in Fig. 10 (a) the breakdowns occurred relatively uniformly throughout the structure, while in Fig. 10 (b) three distinct phases separated by 120° are present. The latter result corresponds to the phase advance per cell of the structure, and similar behaviour has been observed in previous high-gradient tests [23, 43, 44]. This indicates that initially, the high-gradient performance and rate of conditioning of all cells was similar. Following this, from 250 to 450 million pulses, little activity is present due to the reduced operating gradient. In the final 100 million pulses in Xbox-3, the breakdowns occurred predominantly at the structure input.

During the first 100 million pulses in Figs. 10 (d) and (e), when the structure was installed in Xbox-2, the breakdowns once again occurred throughout the structure and at three distinct phases. Tests carried out SLAC have shown that the cleanliness of the structure preparation process affects the number of breakdowns accrued during conditioning [45], and so the contamination associated with the exposure to air during the change in test stands may have contributed to this structure-long spread in breakdown locations. However, from 200 million pulses onwards in Figs. 10 (d) and (e), after the preliminary ramping in gradient had ceased and a pulse length of 200 ns had been reached, approximately 70% of the breakdowns which were accrued had a BD time in the range of 0 to 10 ns, corresponding to the matching cell and the first 6 regular accelerating cells. Several key electromagnetic parameters for the first, central, and final accelerating cells are summarised in Table III.

The breakdown distribution in Fig. 10 (d) is not consistent with the electric field profile which, as shown in Fig. 5, increases in the downstream direction. Notably, S_c and the peak surface magnetic fields are higher in the first few cells. However, visual examinations of previously tested cavities have shown that breakdowns predominantly occur where the surface electric field is highest, not where S_c and the surface

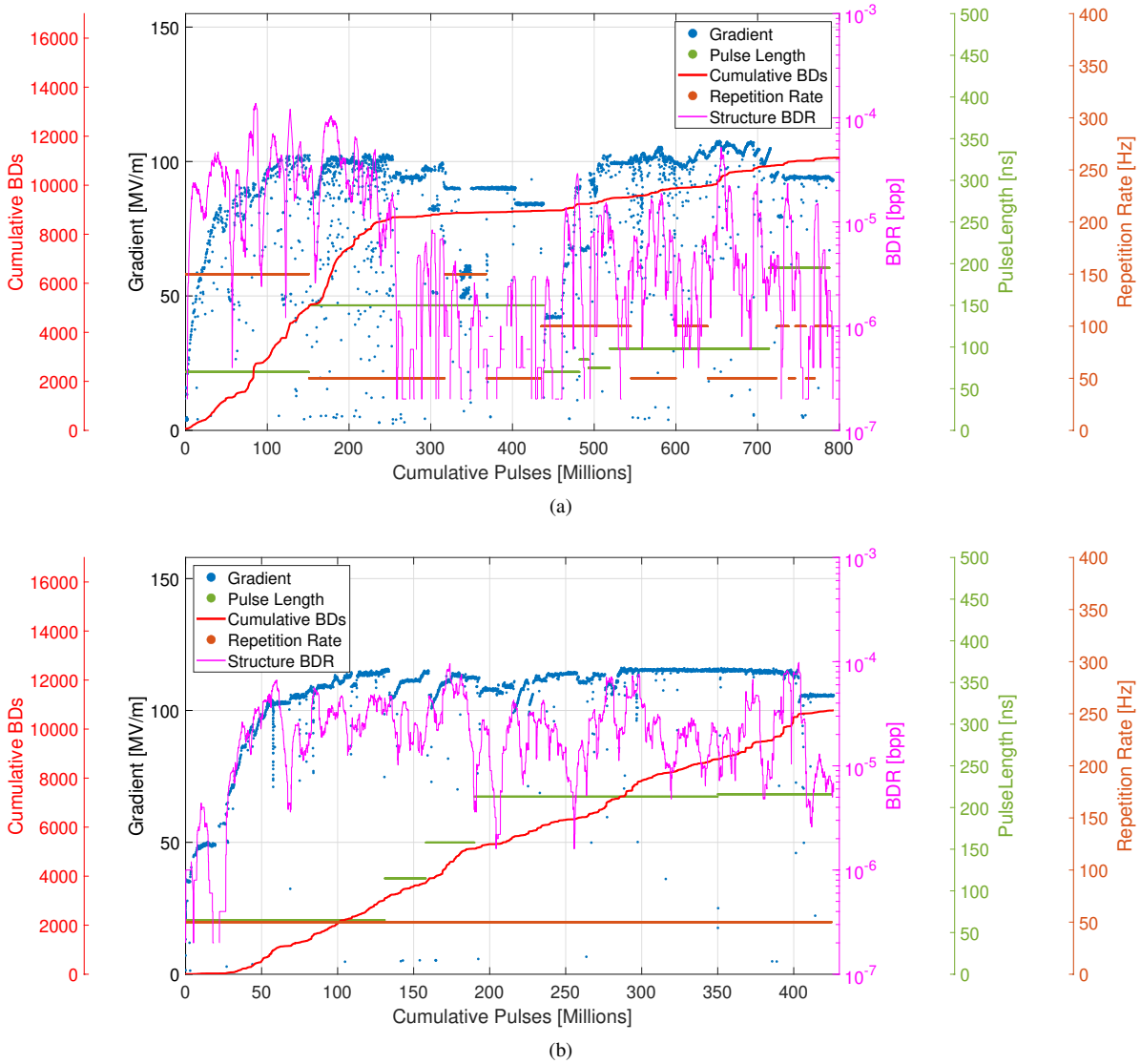

Fig. 9: Conditioning history of the T24 PSI N1 structure while installed in CERN's (a) Xbox-3 and (b) Xbox-2 test stands. Only structure breakdowns are shown. The structure was first installed in Xbox-3 before being moved to Xbox-2 for the remainder of the test.

TABLE III: Electromagnetic parameters for the first, central, and final regular accelerating cells (excluding the couplers) normalized to an accelerating gradient of 1 V/m.

Quantity	First Cell	Central Cell	Final Cell	Units
E_{Surf}/E_{acc}	2	2	2.1	–
H_{Surf}/E_{acc}	2.6	2.45	2.3	A/kV
Sc/E_{acc}^2	0.38	0.33	0.3	A/kV
v_g	1.8	1.305	0.912	$\%c$

magnetic field are highest [23, 46], and so it is unclear if either of these quantities drive the local BDR.

Recently, a "breakdown-loaded electric field" has also been suggested as a potential high-gradient limit [47]. In this theory, it is proposed that the local surface electric field decreases under the loading associated with the acceleration of current emitted in the vicinity of the breakdown site. Areas with a higher propensity for electric field sustenance under loading are then more susceptible to breakdown. This theory predicts that breakdowns in the tapered, CLIC prototype accelerating structures, should occur primarily towards the input in the later stages of testing [47]. However, a quantitative comparison with this theory is not yet possible, as no suggestions have been made as to how the local breakdown rate scales with the breakdown-loaded electric field, and the value is treated only as an ordinal quantity.

Finally, in Figs. 10 (c) and (f) the breakdown phases and spatial locations are plotted against one another. The resulting distributions show that regardless of where a breakdown occurs longitudinally, the difference in phase between incident and reflected signals during breakdowns is an integer multiple of 120°, the phase advance per cell. This indicates that the

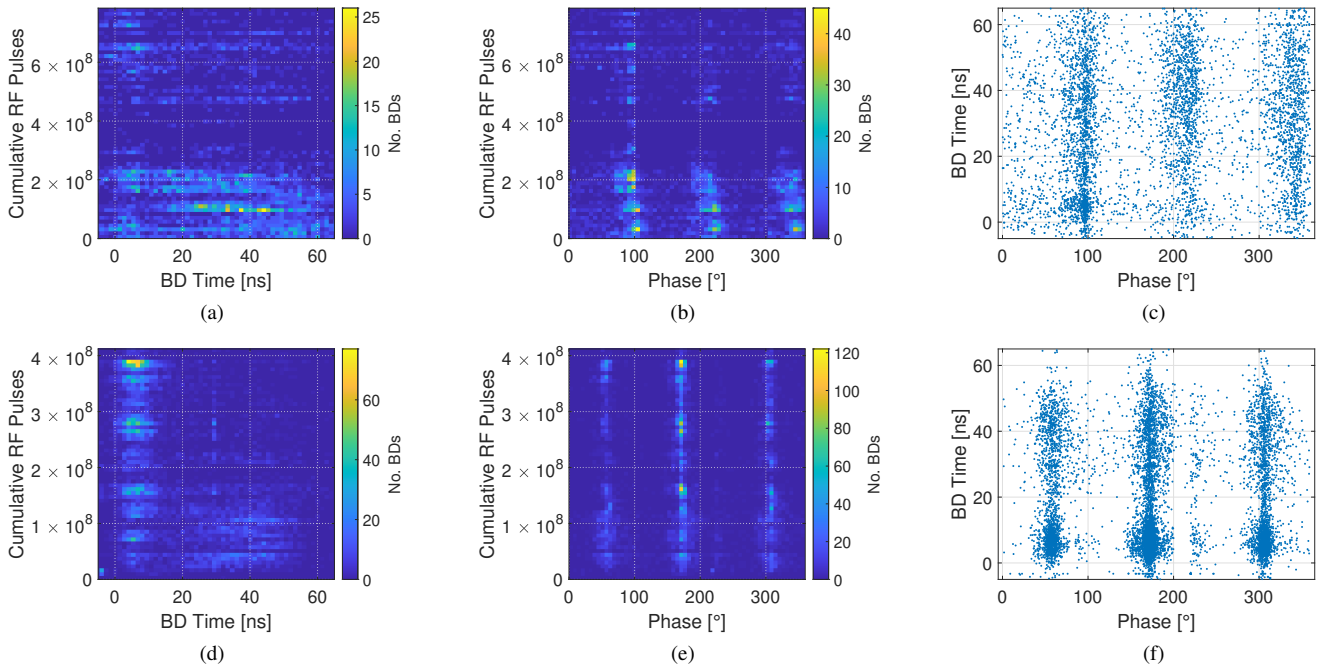

Fig. 10: Breakdown distribution for the T24 PSI N1 structure. On the left side, the longitudinal positions of the breakdowns are shown for the (a) Xbox-3 and (d) Xbox-2 test periods. In the centre, the difference in phase between the incident and reflected signals for the breakdowns in (b) Xbox-3 and (e) Xbox-2 is shown. On the right side, the BD phases are plotted against their longitudinal positions for the (c) Xbox-3 and (f) Xbox-2 test periods. The longitudinal positions are presented in units of ns, referring to the RF signal propagation time. A time of 0 ns corresponds to the structure input while 59 ns (the structure fill time) corresponds to the output coupler.

structure remained well tuned during transport and installation, and throughout both high-power test periods.

VII. High-Power Test of the Second Structure

The second structure test commenced in the Xbox-3 test slot in October 2017. The full conditioning history is presented in Fig. 11. The structure was conditioned algorithmically and reached a gradient of 100 MV/m at an RF pulse length of 60 ns after 105 million pulses. After approximately 180 million pulses, the structure reached an input power of 33 MW at a pulse length 200 ns, corresponding to an accelerating gradient of 93.8 MV/m. The compressed pulse length was reduced, and the operating conditions were held constant for 200 million pulses. On 21st December 2017, after approximately 278 million pulses, the system was switched off for the CERN winter closure. The vacuum integrity of the waveguide network was maintained throughout the pause, and the test was resumed on 9th January 2018. Starting from 400 million pulses on, several ramping periods and changes in pulse length took place. Following this, the structure was once again operated under fixed conditions for the final 75 million pulses of the test. Due to the relatively low BDR and stable operation achieved in Xbox-3, the T24 PSI N2 was also then installed in Xbox-2 for further testing.

The transfer process was similar to that of the T24 PSI N1. In principle, an arrangement in which the vacuum in the structure is maintained could be designed by using, for example, high-power RF windows, as are typically employed in klystron cavities [48–50]. However, such devices can be damaged by high-power operation, breakdowns, and sudden pressure changes, and suitable high-power X-band variants are generally costly, and difficult to design and manufacture [51]. Hence, although the exposure to air necessitates some reconditioning, it is generally preferred due to the associated cost and time savings.

Upon resumption of the test in Xbox-2, the structure was algorithmically ramped up to a target gradient 110 MV/m at an RF pulse length of 50 ns with a BDR setpoint of 3×10^{-5} bpp. Conditioning continued until an accelerating gradient of 110 MV/m was reached at an RF pulse length of 200 ns, after approximately 160 million pulses. As RF breakdown is one of the primary limitations on the achievable gradient several BDR studies were then performed. Beginning after approximately 190 million pulses, the structure was operated under different sets of fixed conditions for the remainder of the test period and the results of these measurements are summarised in Section VII-B. Due to scheduling constraints, the test in Xbox-2 terminated on the 25th September 2018, after the structure had accumulated approximately 661 million high-power pulses over the course of 6 months. Notably, no breakdowns occurred during the final 72 hours ($\approx$13 million pulses) of the test while operating at an accelerating gradient of 101 MV/m and an RF pulse length of 100 ns. This is visible in Fig. 11 when the measured BDR reduces to zero, due to all of the breakdowns having fallen out of the 5 million pulse BDR measurement window.

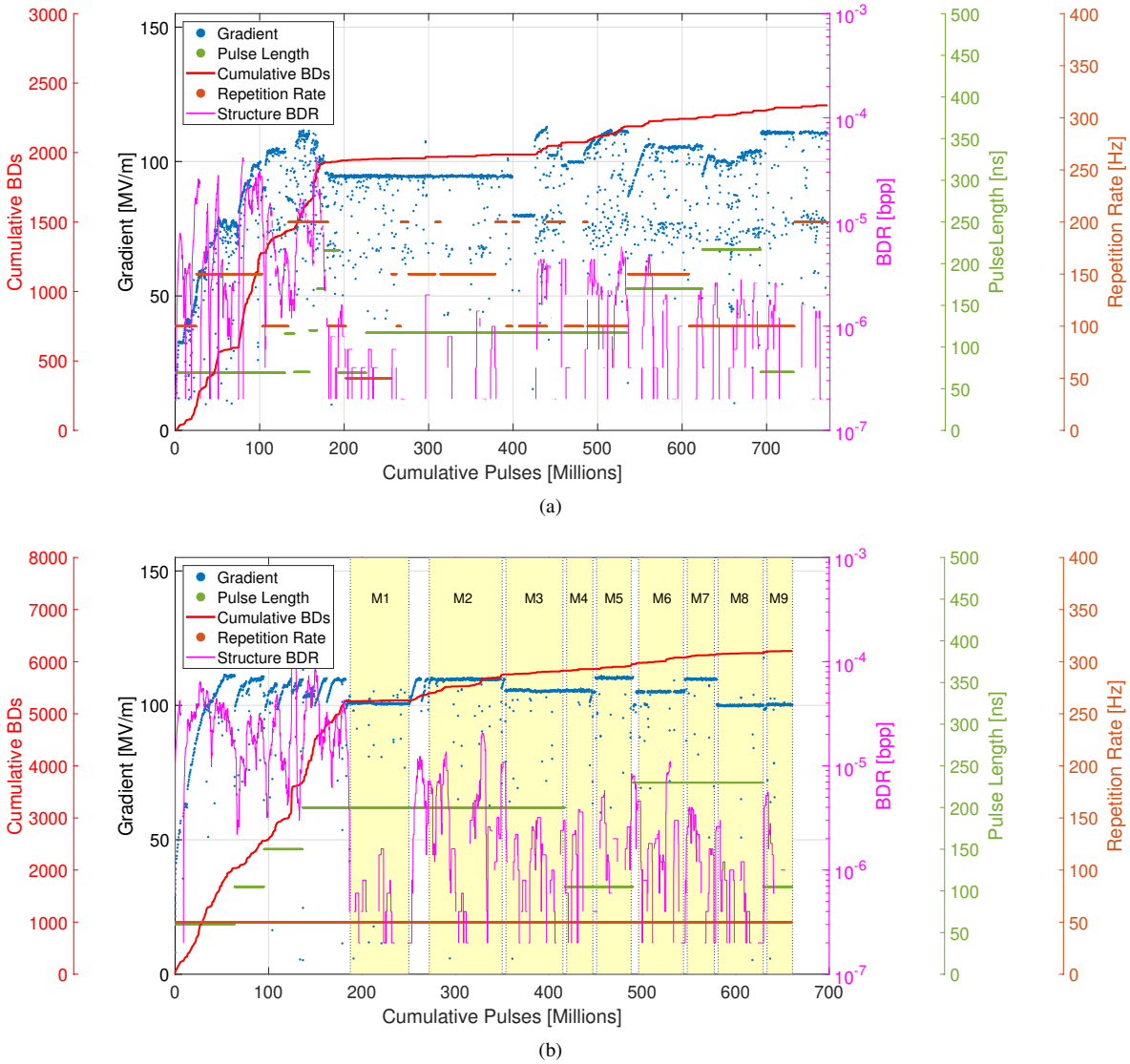

Fig. 11: Conditioning history of the T24 PSI N2 structure while installed in CERN's (a) Xbox-3 and (b) Xbox-2 test stands. The BDR rate measurements that were performed in Xbox-2 are highlighted and labeled from M1 to M9 in (b). Only structure breakdowns are shown.

A. Spatial Distribution of Breakdowns

The spatial distribution of the breakdowns which occurred in the T24 PSI N2 was also monitored during operation. The results for the test periods in the Xbox-3 and Xbox-2 test stands are shown separately in Fig. 12.

Figs. 12 (a) and (b) shows that the breakdowns occurred relatively uniformly throughout the structure, and at all three phases during the first 200 million pulses. The operating gradient was then reduced, resulting in a quiescent period from 200 to 400 million pulses. For the remainder of the test in Xbox-3, the breakdowns occurred predominantly in the early cells and at a single phase. During the first 50 million pulses in Figs. 12 (d) and (e), when the preliminary ramping in Xbox-2 was taking place, activity is once again present along the full length of the structure, and at three distinct phases. Following this, most of the activity takes place at the structure input, with 74% of the breakdowns logged from 200 million pulses onward having times in the 0-10 ns range.

Notably, in Figs. 12 (e) the breakdowns occur predominantly at a single phase after the first 50 million pulses. Contrary to the continuous spread which is visible in Fig. 12 (d), this indicates that the breakdowns occurred either in the same cell, or in the nearby synchronous cells. The discrepancy between these results can be attributed to errors in the time-domain based positioning method, which relies on the emergence of well-defined rising and falling edges in the RF signals. In practice, more indistinct behaviour is often observed in the RF signals during arc formation, resulting in an uncertainty in the measurement, particularly in cavities with short fill times. This was also noted previously, during the test of a dipole-mode X-band RF cavity [46].

In Figs. 12 (c) and (f), where the breakdown phases have

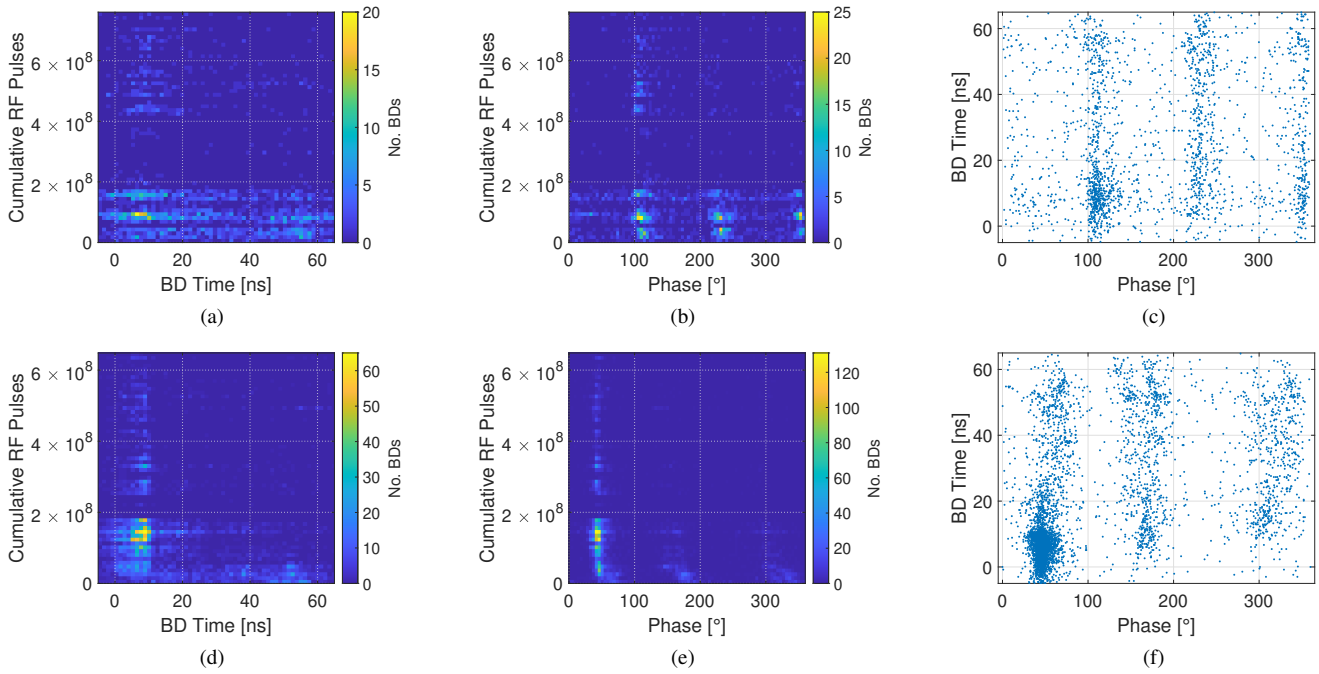

Fig. 12: Breakdown distribution for the T24 PSI N2 structure. On the left, the longitudinal positions of the breakdowns are shown for the (a) Xbox-3 and (d) Xbox-2 test periods separately. Shown in the centre is the difference in phase between the incident and reflected signals for the breakdowns in (b) Xbox-3 and (e) Xbox-2. On the right, the BD phases are plotted against their longitudinal positions for the (c) Xbox-3 and (f) Xbox-2 test periods. The longitudinal positions are presented in units of ns, referring to the RF signal propagation time. A time of 0 ns corresponds to the structure input while 59 ns (the structure fill time) corresponds to the output coupler.

been plotted against the spatial locations, three vertical lines separated by 120° are visible, indicating that, like the T24 PSI N1, the structure remained well tuned throughout the test period.

B. Breakdown Rate Measurements

In room-temperature accelerating structures RF breakdown is one of the primary limitations on the achievable accelerating gradient. As such, the dependence of the BDR on the operating conditions is of great interest, both in the context of feasibility studies and when investigating the underlying physics associated with the phenomenon. Previously, the BDR has been reported as scaling with electric field and RF pulse length as [25]:

$$BDR \propto E^{30} t_p^5 \tag{1}$$

where E is the unloaded accelerating gradient and t_p is the RF pulse length. To investigate these dependencies, the T24 PSI N2 structure was operated under nine accelerating gradient and pulse length combinations after the preliminary conditioning period in Xbox-2. The operating gradients chosen were 101, 105, and 110 MV/m, while the chosen RF pulse lengths were 100 ns, 200 ns, and the pulse designed for the CLIC project, which is comprised of 156 ns flat top and specially designed ramps to compensate transient beam loading for a total pulse length of approximately 240 ns [1]. The pulse shapes used during the tests are shown in Fig. 13. The BDR measurements began after approximately 190 million pulses in Xbox-2 (labelled M1-M9 in Fig. 11), starting with the data points collected at a pulse length of 200 ns. After approximately 415 million pulses the pulse length was decreased to 100 ns and two measurements were performed. Measurements were then taken while operating with the CLIC pulse, followed by a final data point at 100 ns.

In past experiments, it has been shown that it is common for several breakdowns to occur in quick succession, followed by a quiescent period. This observation led to the suggestion that breakdowns may be divided into two distinct groups, "primary" events, the probability of which is largely Poissonian, and "follow-up" events, which are thought to be a consequence of the primary event [42, 52]. In light of this, two breakdown rate values were calculated for each set of operating conditions during the measurement. The first, referred to as the *total BDR*, was calculated as the total number of breakdowns divided by the total number of RF pulses for each measurement window. The second rate, referred to as the *primary BDR*, was calculated by excluding all breakdowns which occur within 3000 pulses of the previous breakdown (corresponding to one minute of pulsing at 50 Hz). The primary BDR is then equal the total BDR divided by the average number of breakdowns which occur within 3000 pulses of one another. The calculation of a primary BDR also serves as a means of excluding anomalous events in which large number of breakdowns occur in quick succession, which could otherwise

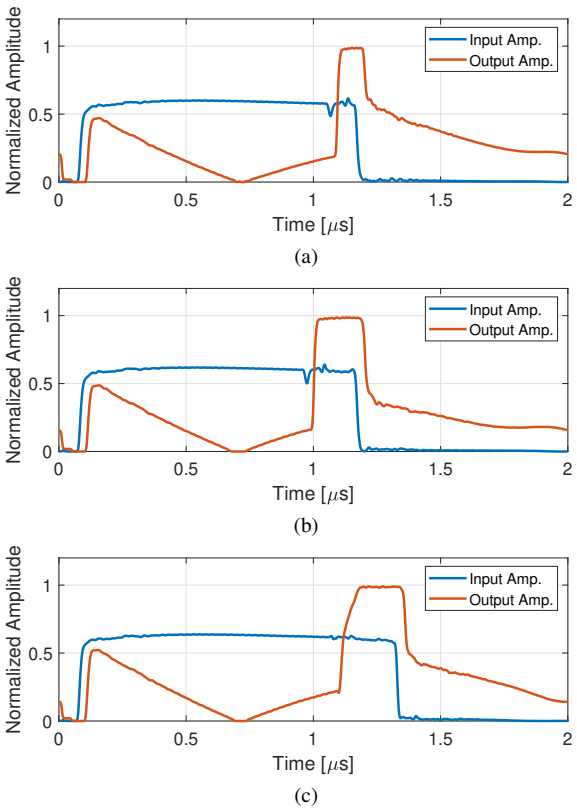

Fig. 13: The 100 ns (top), 200 ns (centre), and CLIC (bottom) pulse shapes used during the BDR measurements performed in Xbox-2 with the T24 PSI N2 structure. The RF pulse shapes before (Input Amp.) and after (Output Amp.) compression are both shown.

dominate the statistics at low BDRs.

Throughout the BDR measurements, several studies pertaining to the field emitted current within the structure were performed. In these measurements, the pulse length was reduced to ≈10 ns for a period of 3-4 minutes several times per week. Approximately, 0.15% of the total pulses recorded during the BDR measurements were of this type, and as the operating conditions were changed, these measurement periods have been excluded in the calculation of the total and primary BDRs. The results of these studies have been previously reported in detail [53]. Where relevant, any ramping in power required to reach the target operating gradient between measurements has also been excluded. The most notable example of this is visible in Fig. 11 (b), between the first and second BDR measurements, labelled M1 and M2 respectively. The results of the measurements, and the order in which they were performed, are summarised in Table IV.

In Eq. 1 the BDR is shown to scale much more strongly with the applied electric field than with the pulse length, and the relevant exponents are often obtained by fitting to sets of gradients (or operating powers) and pulse lengths separately [30, 46, 54, 55], as opposed to fitting to the product of the two. As such, power law fits were applied to both the total and primary BDRs for each gradient and pulse length measurement set separately. Measurements with the same pulse length (e.g. M1, M2, and M3 in Fig. 11) were fit to a power law relation of the form:

$$BDR(E) = a \cdot E^b \tag{2}$$

where a is a constant and b is the power law exponent. Similarly, measurements combinations in which the gradient was fixed (e.g. M2, M5, and M7) were fit to:

$$BDR(t_p) = c \cdot t_p^d \tag{3}$$

where c and d are the fitting coefficients. It is worth noting that although an empirical pulse length dependence has been previously reported, a dependence on the pulse shape has not. Although the FWHM of the CLIC pulse is approximately 240 ns, the total energy is less than that of a 240 ns rectangular compressed pulse and, as the irregular shape has not been accounted for, the resulting fits may be affected. However, the result may nonetheless offer some insight into how the pulse shape affects the BDR, and into what could be considered an "equivalent pulse length". The coefficients for the resulting fits are summarised in Table V and plotted, alongside the data, in Fig. 14.

TABLE IV: Summary of the BDR measurements performed in Xbox-2. Breakdowns which occur within 3000 pulses of the previous breakdown are excluded in the calculation of the primary BDR. The first column refers to the order in which the measurement was carried out.

No.	Gradient [MV/m]	t_p [ns]	Pulses [$\times 10^6$]	BDs	Primary BDs	BDR [bpp]
M1	101	200	62	20	15	3.24E-07
M2	110	200	77	350	116	4.53E-06
M3	105	200	60	66	31	1.09E-06
M4	105	100	34	35	17	1.04E-06
M5	110	100	40	94	33	2.38E-06
M6	105	≈ 240	47	106	42	2.28E-06
M7	110	≈ 240	32	50	29	1.54E-06
M8	101	≈ 240	50	20	12	4.06E-07
M9	101	100	27	12	5	4.39E-07

The 100 ns, 200 ns, and CLIC pulse data sets shown in Fig. 14 (a) were found to scale with $E^{20.97}$, $E^{31.14}$, and $E^{30.05}$ respectively. The exponents for the 200 ns and CLIC pulse data sets are within 3.8% and 0.17% percent of the reported value, while the exponent for the 100 ns set is ≈30% lower. Given that the final 101 MV/m data point for the 100 ns data point was taken last, a larger exponent should be expected if the structure had continued to condition throughout the measurements. However, prior to recording the final 100 ns data point at 101 MV/m (between measurements M8 and M9), several breakdowns were intentionally induced as part of one of the previously referenced field emission experiments [53]. A close-up of the conditioning history in this region is shown in Fig. 15.

The majority of the breakdowns in the final measurement occurred within the first 5 million pulses, immediately following the field emission measurements shown in Fig. 15.

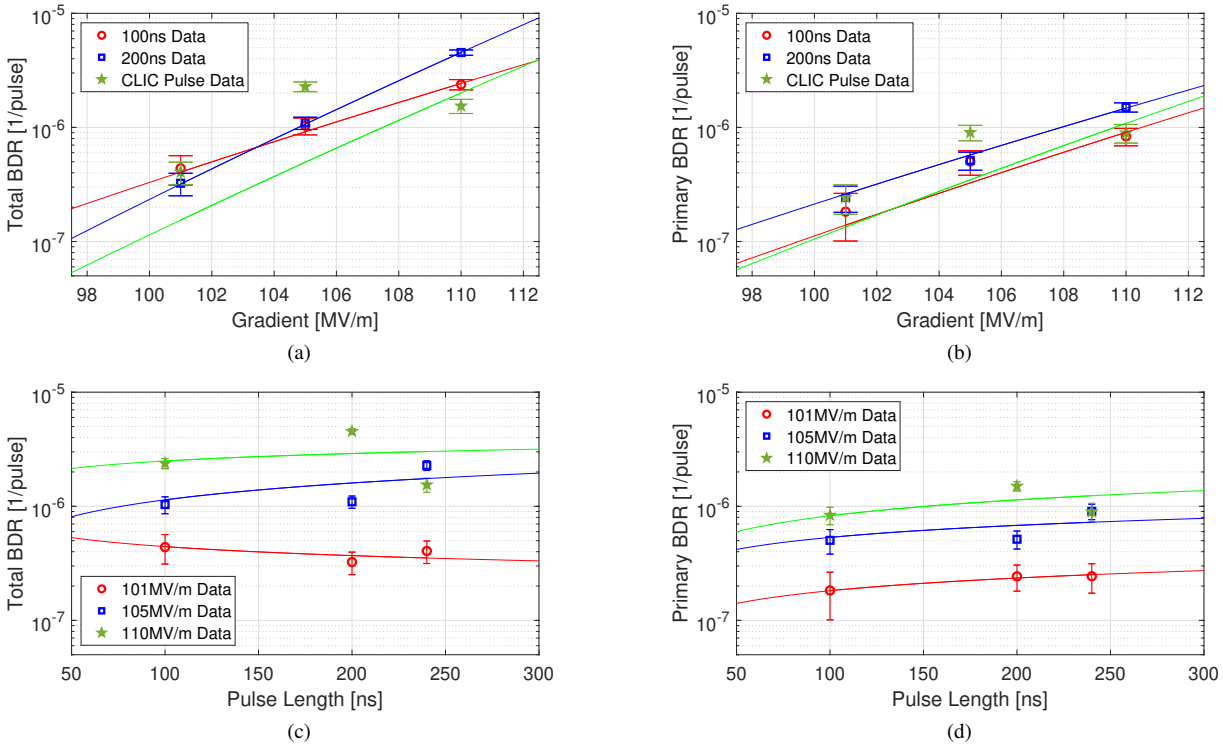

Fig. 14: The total and primary BDRs as a function of RF pulse length and accelerating gradient for the T24 PSI N2 structure tested in CERN's Xbox-2 test stand. In the upper plots, the (a) total and (b) primary BDRs are plotted against the unloaded accelerating gradient for different RF pulse lengths. In the lower plots, the (c) total and (d) primary BDRs are plotted against the RF pulse lengths for different unloaded accelerating gradients. Error bars have been calculated as the square root of the total number of breakdowns or primary breakdowns for each data point.

It is speculated that some damage accrued during these measurements may have resulted in further breakdowns later, contributing to the initially elevated BDR. Additionally, no breakdowns occurred during the final three days of operation, corresponding to approximately 13 million pulses. Given that measurement M9 had fewer total pulses than all the others, a longer measurement period may then have resulted in an exponent closer to the reported value.

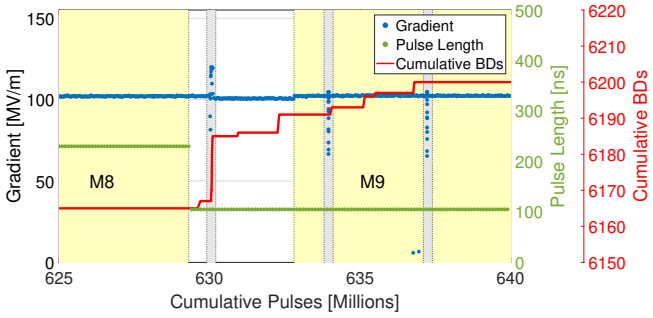

Fig. 15: Close-up of the T24 PSI N2 conditioning curve between measurements M8 and M9. The positions of the field emission measurements are shown by the grey bars. To induce several breakdowns, the operating gradient was briefly increased at the 630 million pulse mark.

For the 200 ns and CLIC pulse data sets, the exponents obtained by fitting Eq. 2 to the primary BDRs are 35% and 18% lower than those associated with the total BDRs. Were the probabilistic behaviour the same at all gradients, the primary BDRs would all be reduced by a constant factor. The fact the exponents obtained by fitting Eq. 2 to the primary BDRs are lower, shows that the data points recorded at the higher gradients have been reduced more, indicating that, on average, more follow-up breakdowns can be expected when operating at higher gradients.

Notably, for the CLIC pulse data set the highest total and primary BDRs were recorded while operating at 105 MV/m. This result contradicts the empirical relationship between the electric field and the BDR given in Eq. 1, and has resulted in sum of squared errors (SSE) values which are more than a order of magnitude higher than the others, and in a negative R^2 value. This indicates that the SSE is greater than two times the sum of squares total (SST), meaning the fit is extremely poor. This feature is also likely exacerbated by the limited number of data points.

When the results are plotted as a function of pulse length, the exponents of the fits are less than 11% of the reported value. Additionally, the confidence intervals are large, with most being more than an order of magnitude higher than the exponents themselves, suggesting that the measurements likely do not represent the true scaling well. Additionally, a negative exponent was recorded for the 101 MV/m data set,

as the data point at 100 ns (measurement M1) was higher than the others, a result which contradicts the expected behaviour. However, as noted previously, the BDR for this point could be, in part, attributed to the field emission measurements shown in Fig. 15. As such, several other facets of operation should likely be considered when addressing the dependence of the breakdown rate on the pulse length or the gradient, such as the conditioning history, the order in which measurements are carried out, and indeed the pulse shape, as opposed to the length alone.

Finally, it is worth discussing the significance of the results in the context of the CLIC project. As stated in Section I, the CLIC target BDR is 3×10^{-7} bpp/m. In the T24 PSI structure, the length of the regular accelerating section is ≈20 cm, and so the corresponding target for this section is 6×10^{-8} bpp, equating to one breakdown per 16.67 million pulses. Although the total BDRs for the measurements summarised in Table IV were all above this value, only a single breakdown was accrued during the final 17 million pulses of measurement M8, while operating with a CLIC pulse at 101 MV/m. However, it should be noted the field profile differs depending on whether or not the structure is loaded with a beam, and a higher input power is required to establish same operating gradient while loaded [1]. Additionally, due to the cessation of measurement M8, and intentional induction of breakdowns during the measurements shown in Fig. 15, it is not known how the breakdown rate would have evolved had the structure continued operating under these conditions.

C. Probabilistic Behaviour of Breakdowns

It has been reported that the probabilistic behaviour of breakdowns may be described by the sum of two exponential terms, as [42, 52]:

$$PDF(n_p) = Ae^{-\alpha n_p} + Be^{-\beta n_p} \tag{4}$$

where PDF is the probability density function of the number of pulses between subsequent breakdowns, n_p. In this fit, α corresponds to the long-term, largely Poissonian behaviour of primary breakdowns, while β refers to the follow-up breakdowns, and A and B are constants to facilitate fitting to experimental data. Previously, this relation was shown to describe the behaviour of a DC electrode operated at three different voltage and pulse length combinations, and a 12 GHz high-gradient cavity [52]. The α and β values obtained by fitting to these data sets ranged from 0.73×10^{-5} to 22.22×10^{-5} and from 0.8851×10^{-3} to 2.187×10^{-3} respectively, indicating that, although the coefficients are affected by the operating conditions, Eq. 4 is applicable to a wide variety of data sets [42, 52]. However, the dependence of these coefficients on, for example, the pulse length, the operating field, and the level to which the device has been conditioned, is not well understood.

To examine the probabilistic behaviour during the test, and to complement and compare with previously presented results [42, 52], PDF distributions have been calculated for the T24 PSI N2. The number of pulses between subsequent breakdowns was first calculated for the structure test data. k quantiles were then used to determine bin widths, $\Delta_{bin,i}$, for the distribution such that each bin contained the same number of samples, N_{bin}. The PDF, $f(n_p)$, was then calculated as the number of events per unit bin, normalized to ensure integral of the distribution is unity, i.e:

$$f(n_{p,i}) = \frac{1}{\sum_{j=1}^{k-1}\left(N_{bin}/\Delta_{bin,j}\right)} \cdot \frac{N_{bin}}{\Delta_{bin,i}} \tag{5}$$

Distributions were first calculated for the entirety of the T24 PSI N2 structure tests in Xbox-3 and Xbox-2 separately and Eq. 4 was fit to the results. Treating data sets M1-M9 generally resulted in poor fits due to the low number of breakdowns which were accrued during each of the measurements. Instead, to provide a more general indication as to whether the probabilistic behaviour changes during high-gradient, low-BDR operation, the distribution was calculated for the sum of these data sets.

The resulting PDFs, and their corresponding fits, are shown in Fig. 16 and the fitting coefficients are summarised in Table VI. Previously, it has also been shown that breakdowns which occur in quick succession are more likely to occur spatially close together [52], and so to complement the PDFs, the spatial displacement between subsequent breakdowns has been calculated, and is also plotted against the number of pulses since the previous breakdown for each of data sets.

As shown in Fig. 8, the voltage is ramped back up towards the set value after breakdowns. Consequently, the first PDF gradually increases during the first few hundred pulses during this ramping period. As this is thought to be a consequence of the control system, and not an in inherent feature of breakdown itself, the lower bound for the fitting was set to the peak of the PDF. The choice of where to place the upper bound is somewhat arbitrary. As a compromise between readability, and obtaining a reasonable fit, the upper bound was selected such that the fit would be applied to 80% of the data. In Figs. 16 (a), (c), and (e), the x-axis has been drawn to show 85% of the total data, so as to demonstrate the increasing divergence between the fit in the later regions. As a consequence of the low BDRs achieved during measurements M1-M9, the x-axis in Fig. 16 (e) is an order of magnitude larger than others.

For each data set, 101 quantiles were used, resulting in the data being placed into 100 bins. Hence, each point in Fig. 16 represents 1% of the total data. To ensure a good fit was achieved over the full range, the points were also weighted during the fitting process. The weighting factor for each bin was calculated as its height multiplied by its width, divided by the maximum bin height. By doing so, a reasonable fit is also obtained in the low density, later part of the distribution, where the corresponding error terms are an order of magnitude smaller than those associated with the points at the start of the distribution.

In the inset plot in Fig. 16 (a), the peak of the probability distribution (shown by the grey dashed line) occurs later than in Figs. 16 (d), and (e). This shift may be attributed to a change in the control system between test stands, with Xbox-2 having

TABLE V: Summary of the results of fitting Eqs. 2 and 3 to the sets of gradient and pulse width BDR measurements presented in Table IV. For each fit, the sum of the squared errors (SSE) and the coefficient of determination (R^2) are also provided.

	Total BDR				**Primary BDR**			
Data Set	**a**	**b**	**SSE [$\times 10^{-15}$]**	R^2	**a**	**b**	**SSE [$\times 10^{-15}$]**	R^2
t_p= 100 ns	4.087e-49	20.97±0.05	45.51	0.977	1.883e-51	21.94±0.17	101.2	0.5249
t_p= 200 ns	1.377e-69	31.14±0.1	4.795	0.9995	4.852e-48	20.31 ±0.05	11.37	0.9871
$t_p \approx$ 240 ns	2.448e-67	30.05 ±0.46	15390	-7.631	1.773e-56	24.51 ±0.34	1092	-2.809
Data Set	**c**	**d**	**SSE [$\times 10^{-15}$]**	R^2	**c**	**d**	**SSE [$\times 10^{-15}$]**	R^2
E=101 MV/m	1.485e-06	-0.26±3.35	4.953	0.2863	3.323e-08	0.37±1.11	0.1308	0.9464
E=105 MV/m	8.963e-08	0.54 ±11.54	529.8	0.4622	1.064e-07	0.35 ± 8.34	60.72	0.4157
E=110 MV/m	9.246e-07	0.22 ± 16.02	4857	-0.02026	9.795e-08	0.46±10.5	250.8	0.08

been set to ramp back up in power more quickly then Xbox-3 following breakdowns. The use of different control system settings, and conditioning algorithms, then makes data sets less comparable, and warrants attention in future experiments. Examining the coefficients in Table VI shows that the α term is highest for the entirety of the Xbox-2 data set. However, during the test period in Xbox-3, the pulse compressor accrued breakdowns regularly and thus contributed to the measured BDR, significantly slowing the rate at which the input power was increased by the test stand control system. Conversely, few breakdowns occurred in the pulse compressor during the test period in Xbox-2. It is, therefore, unclear to what extent the pulse compressor may have affected the probabilistic behaviour in Xbox-3.

As mentioned, fits to DC electrode and X-band accelerating structure tests have previously been reported with α values ranging from 0.73×10^{-5} to 22.2×10^{-5}, and β values ranging from 0.8851×10^{-3} to 2.187×10^{-3} [52]. The β value associated with the Xbox-2 data set is higher than in previous tests, though this may be attributed to the flat runs resulting in a reduced number of primary BDs. Otherwise, the exponents associated with the T24 PSI N2 data fall within the range of previously reported values, meaning the structure's high-gradient behaviour is similar to that of other high-field devices.

In Fig. 16 (b), where the number of pulses between subsequent breakdowns is plotted against the difference in their longitudinal positions, the density of points increases close to the temporal and spatial origins. This indicates that it is unlikely for breakdowns which occur in quick succession to occur spatially far apart. In Figs. 16 (d) and (f) however, the majority of the points are close to the x-axis, even in the later portions of the distribution. As was shown in Fig. 12 (d), the majority of the breakdowns in Xbox-2 occurred predominantly towards the structure input and so the distributions in Figs. 16 (d) and (f) reflect this result.

To provide an indication of how many follow-up breakdowns can typically be expected after a primary breakdown, and how long successions of breakdowns are likely to last, a PDF of the number of breakdowns which occur within 3000 pulses was also calculated. As in Table IV, breakdowns which occur within 3000 pulses of the previous breakdown are counted as one event. The events were binned by the number of breakdowns they were comprised of and the PDF was calculated by dividing each bin by the total number of events, thus ensuring the sum of the distribution is equal to one. The first bin, centred on one, then refers to the probability of a primary breakdown having no follow-up breakdowns. The second bin, centred on two, is the probability that a primary breakdown has a single follow-up breakdown. The resulting PDFs are shown in Fig. 17.

In each data set, the distribution for the number of breakdowns per event shows that the most likely individual result is the occurrence of a single, primary breakdown. For the Xbox-3 and Xbox-2 data sets, 66% and 52% of the events were of this kind respectively. Conversely, 45% of the events in M1-M9 data set were comprised of a single, primary breakdown, with the remaining 55% of the distribution being spread among the higher values. Hence, in the M1-M9 data set the majority of primary breakdowns were accompanied by follow-ups.

Finally, the distributions for the Xbox-2 and M1-M9 data sets in Fig. 17 are generally higher, and extend further right, than the distribution for the Xbox-3 data set, showing that follow-up breakdowns were more likely during the test in Xbox-2. The mean number of breakdowns per event was found to be 1.8, 2.8, and 2.5, for the Xbox-3, Xbox-2, and M1-M9 data sets respectively.

VIII. Effect of Exposure to Air

Occasionally, maintenance and interventions necessitate venting the waveguide network in high-gradient facilities. Additionally, it has been previously been suggested that when

TABLE VI: The results of fitting Eq. 4 to the PDFs of the number of pulses between subsequent breakdowns.

Data Set	**Pulses [$\times 10^6$]**	**No. BDs**	**A [$\times 10^{-4}$]**	α**[$\times 10^{-5}$]**	**B [$\times 10^{-2}$]**	β**[$\times 10^{-3}$]**	**SSE [$\times 10^{-5}$]**	R^2
Xbox-3	772	2340	4.868 ±0.909	2.26± 0.424	4.389 ± 1.162	1.611 ± 0.249	9.09	0.8811
Xbox-2	660	6205	3.075±0.938	14.1 ± 3.61	2.373 ±0.534	5.812±0.959	2.442	0.8398
M1-M9	429	753	1.496 ± 0.464	3.227 ± 0.816	3.85±0.96	4.839 ±0.878	1.639	0.7829

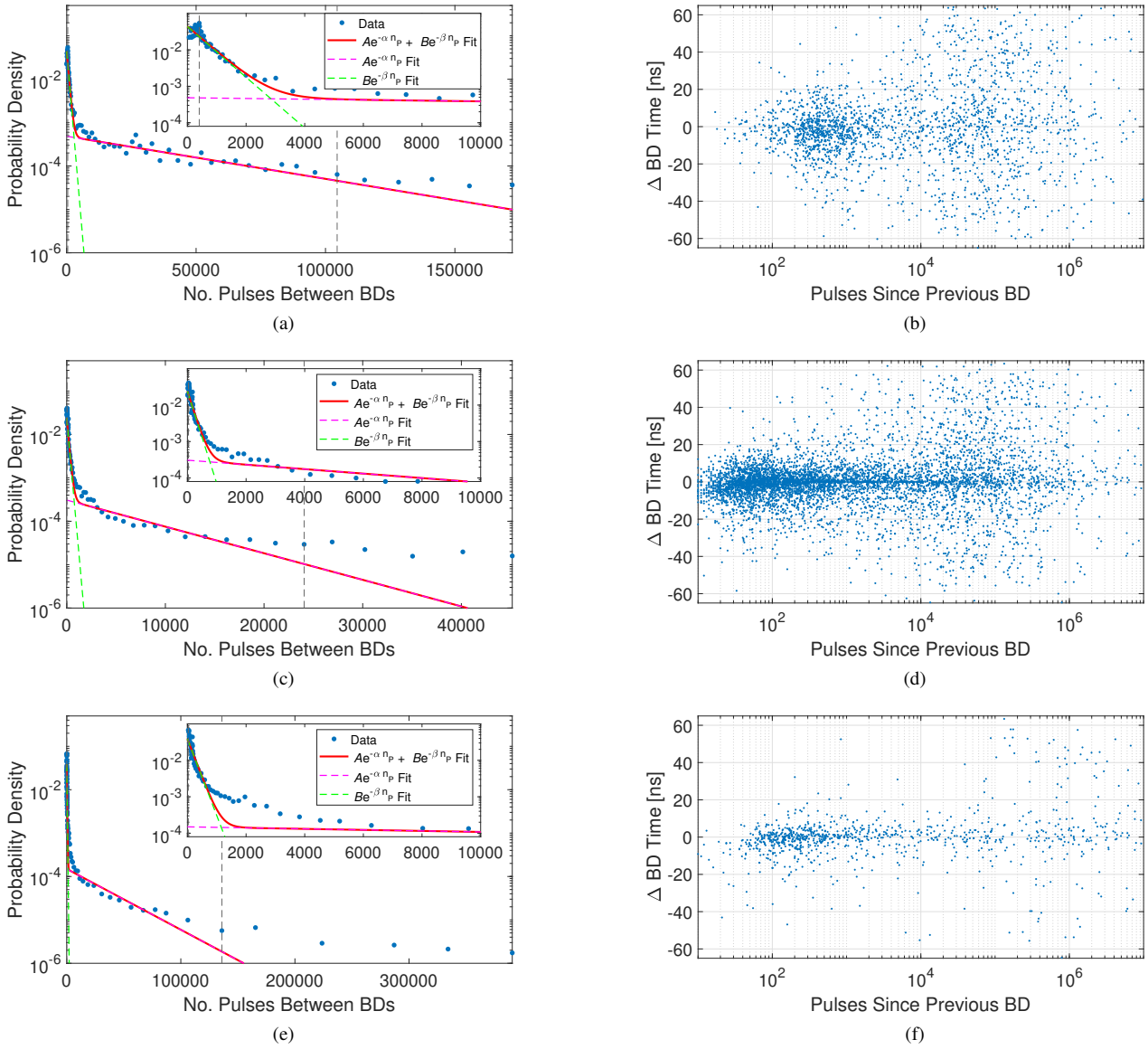

Fig. 16: PDFs of the number of pulses between subsequent breakdowns for the (a) Xbox-3 test period, (c) the Xbox-2 test period, and (e) measurements M1 to M9. The range in each PDF to which Eq. 4 was fit is delineated by the dashed grey lines. On the right side, the longitudinal distance between each pair of successive breakdowns is plotted as a function of number of pulses between them for the (b) Xbox-3 test period, (d) the Xbox-2 test period, and (f) measurements M1 to M9. The distance between successive breakdowns refers to the difference in the signal propagation time and has units of nanoseconds. If two successive breakdowns occur in the same location this quantity adopts a value of zero.

manufacturing high-field components, a pre-conditioning strategy in which structures are conditioned in a purpose-built facility prior to installation in a beam line may be adopted, as opposed to being conditioned in situ [19, 56]. As such, the effect of exposure to air is of interest both in an operational context, and when determining the feasibility of the latter scheme. While transferring the T24 PSI N1 and N2 structures from Xbox-3 to the Xbox-2 test slot, each was exposed to air. The number of RF pulses, and breakdowns, required for each structure to reach operation at 100 MV/m is shown in Fig. 18 for both Xbox-3 and in Xbox-2.

The T24 PSI N1 structure required approximately 100 and 50 million pulses to reach an accelerating gradient of 100 MV/m in Xbox-3 and Xbox-2 respectively, while the number of breakdowns accrued in each case was ≈3000 and ≈500. Additionally, When reinstalled in Xbox-2 the structure was capable of recommencing operation at a markedly increased gradient. These results indicate that the conditioned state of the surface had been at least partially been retained upon exposure to air. The T24 PSI N2 structure reached an accelerating gradient of 100 MV/m in 32 million pulses in Xbox-2, approximately one third of the ≈100 million pulses initially required in Xbox-3. However, a similar number of breakdowns were accrued during the initial ramping in Xbox-2. As men-

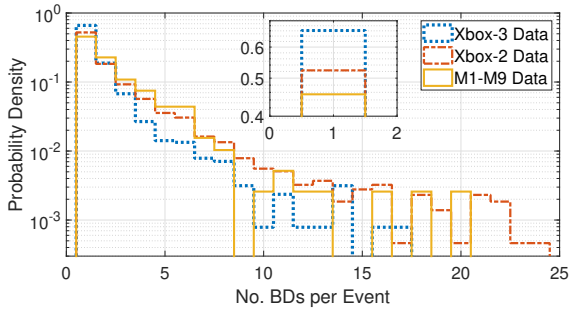

(a)

Fig. 17: Distributions of the number of pulses per event for different portions of the T24 PSI N2 test. The heights of the first bars are 0.66, 0.52, and 0.45 for the Xbox-3, Xbox-2, and M1-M9 data sets respectively (shown in the inset plot).

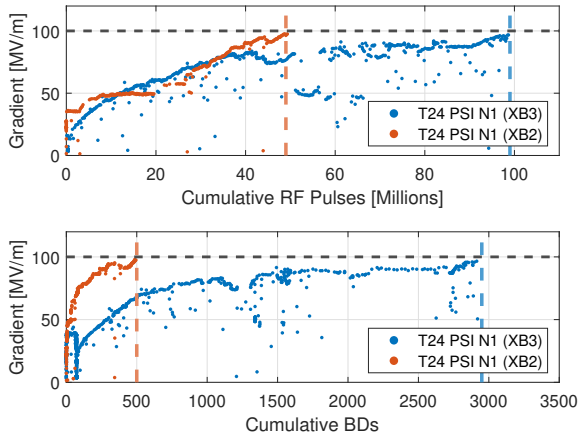

(a)

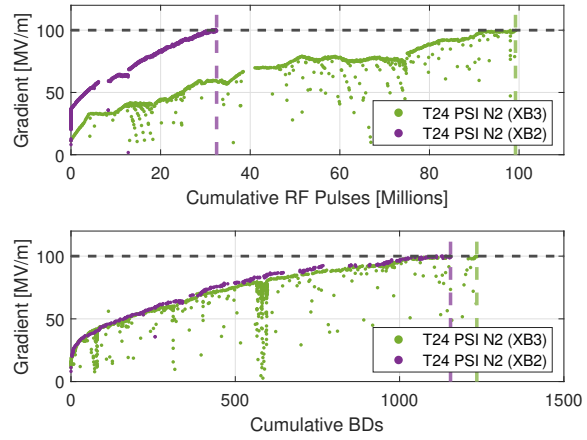

(b)

Fig. 18: Conditioning curves of the T24 PSI N1 (a) and N2 (b) in Xbox-3 and Xbox-2. The number of pulses and breakdowns required to reach operation at 100 MV/m are shown by the vertical dashed lines.

tioned briefly in Section VII-C, the pulse compressor accrued breakdowns regularly during the test in Xbox-3, contributing to the measured BDR and reducing the rate at which the input power was increased by the test stand control system. As such, the structure was effectively conditioned at a lower BDR set point in Xbox-3, and it is not known if this affected the results shown in Fig. 18 (b). Despite this, both structures were once again capable of stable, high-gradient operation, indicating that although the short exposure period necessitated some reconditioning, it did not permanently reduce the structures' propensities for high-power operation.

IX. Posttest Measurement

After removal from the Xbox-2 test slot further low-power RF measurements were performed to examine the effect of high-power operation on the field distribution and overall tuning of the structure. A comparison between the pre and post-test measurements is shown in Fig. 19. After the high-power tests, the measured S_{11} for both structures was still below -30 dB at the operating frequency. The results from the bead pull showed that the average phase advance per cell of the first structure had increased by 0.08°, while a decrease of 0.14° was observed in the second. Consequently, the error on the average phase advance always remained within 0.08°of the target, 120° value. This value is comparable to what is typically achieved during tuning procedures, with previous X-band structures having been tuned such that the average phase advances is within 0.1° of the design value [12, 28, 57]. The average change in the electric field profile was 0.033% and -0.50% in the first and second structure respectively.

In 2018, a TD26R05 structure was conditioned up to an unloaded gradient of 110 MV/m at a compressed pulse length of 170 ns over the course of 900 million high-power pulses. During the test, the structure accrued a total of 23000 breakdowns, and ultimately reached a BDR of 2×10^{-5} bpp/m [43]. Post-test measurements of this structure showed that its S_{11} value had increased from -58 dB to -26 dB, whilst the field profile and phase advance for each cell were recorded as having deviated by ±5% and ±4° respectively [43]. The results of the T24 PSI structures also suggest that high-power operation results in measurable detuning, though despite the long test period and significant number of breakdowns accumulated, only comparatively minor changes in the structures' S-parameters were observed, indicating that long-term reliable operation is nonetheless feasible with structures of this kind.

X. Conclusion

To avoid the need for tuning after structure fabrication, two novel X-band accelerating structures based on an existing CERN design have been fabricated using SwissFEL production methods and tested at CERN's high-gradient test facility. Low-power RF measurements showed that the field distribution was as expected and average phase per cell of each structure was within 0.6° of the design value, similar to what is typically achieved in structures which have been subjected to tuning procedures.

In CERN's Xbox-3 and Xbox-2 test stands, both structures were conditioned up to unloaded accelerating gradients in excess of 100 MV/m at various RF pulse lengths, showing that

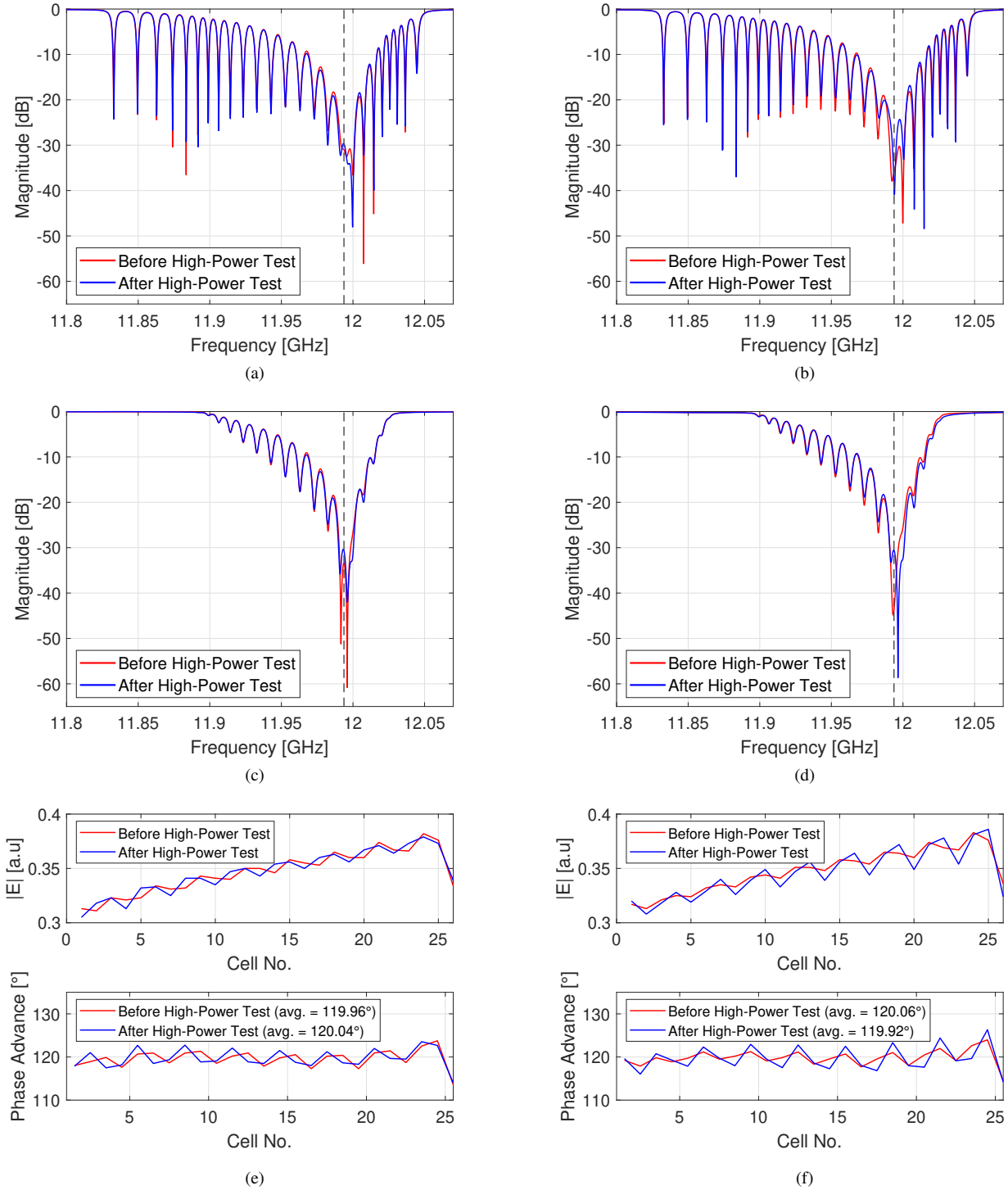

Fig. 19: Results of the S-parameter and bead pull measurements for the T24 PSI N1 and the T24 PSI N2 structures from before and after the high-power test. On the left side, the results of the (a) S_{11}, (c) S_{22}, and (e) bead pull measurements of the PSI T24 N1 structure are shown. On the right side, the results of the (b) S_{11}, (d) S_{22}, and (f) bead pull measurements of the PSI T24 N2 structure are shown.

structures' performances were comparable to previous CLIC prototypes. During the second structure test, measurements were performed to investigate the dependence of the BDR on the accelerating gradient and the RF pulse length. The results indicate that the BDR scales strongly with the electric field, with the corresponding power law fits having exponents ranging from 20.97 to 31.14. When the same power law fit was applied to the primary BDR, the corresponding exponents were generally lower, ranging from 20.31 to 24.51. This indicates that, on average, the number of follow-up breakdowns which can be expected after a primary breakdown increases with the operating gradient.

However, when the results were plotted as a function of RF pulse length the quality of the fits was poor. Only three data points were recorded during operation, and so to obtain more accurate estimate of how the BDR scales with the pulse length, additional pulse length measurements are likely required. It is also worth noting that in one of the RF pulses used was a CLIC pulse, as opposed to a standard rectangular pulse The effect of using alternative RF pulse shapes or ramps, as opposed to sharp rising edges, is an aspect of operation which warrants further investigation in future studies. In light of this, it is recommended that additional measurements be made to better ascertain how the BDR is affected by the length and shape of the RF pulse.

Notably, only one breakdown was accrued during the final 17 million pulses of the penultimate BDR measurement of the PSI T24 N2 in Xbox-2, while the structure was operated at a gradient of 101 MV/m with a CLIC pulse shape. This corresponds to a BDR of approximately 5.9×10^{-8} bpp, and when adjusted for the structure length, meets the 3×10^{-7} bpp/m target for the CLIC project. Post-test RF measurements demonstrated little change in the RF properties of the structures, indicating that little degradation occurred during high-power operation and transport, despite the relatively large number of RF pulses and breakdowns accrued.

The success of the structure fabrication and high-power tests presented in this paper demonstrate the viability of the tuning-free, vacuum brazed PSI technology. Although the structure was designed in the context of the CLIC study, the technology is attractive in a range of applications, particularly in facilities which lack the RF expertise for structure tuning, and in longer, multi-structure arrangements where structure tuning would otherwise necessitate a significant cost and time investment.

Given the high achievable accelerating gradient, the technology is also attractive in applications where the accelerator size and the associated infrastructural costs are key constraints such as compact photon sources, future FELs, and radiotherapy facilities. Two examples where the use of X-band cavities is already planned are the Smart*Light project [58], a compact and transportable hard X-ray inverse Compton scattering source, and the CompactLight study [59], a collaboration established to design a next-generation FEL with a lower cost and size than existing facilities. Additionally, the use of very high-energy electron (VHEE) beams in the range 50–250 MeV has recently been studied as a potential radiotherapy option for the treatment of deep-seated tumors, and this is another application to which the technology is well-suited [8, 60–62].

REFERENCES

[1] M. Aicheler *et al.*, "A Multi-TeV Linear Collider Based on CLIC Technology: CLIC Conceptual Design Report," CERN, Geneva, Switzerland, Tech. Rep. CERN-2012-007, 2012, 10.5170/CERN-2012-007.

[2] A. Vnuchenko *et al.*, "High-gradient testing of an S-band, normal-conducting low phase velocity accelerating structure," *Phys. Rev. Accel. Beams* Vol. 23, Iss. 8, pp. 084801, Aug. 2020, 10.1103/PhysRevAccelBeams.23.084801.

[3] A. Degiovanni *et al.*, "High-Gradient test results from a CLIC prototype accelerating structure:TD26CC," in *Proc. of the 5th International Particle Accelerator Conference (IPAC2014),* Dresden, Germany, 2014, pp. WEPME015, 10.18429/JACoW-IPAC2014-WEPME015.

[4] W. Wuensch *et al.*, "Fabrication and high-gradient testing of an accelerating structure made from milled halves," in *Proc. of the 28th Linear Accelerator Conference (LINAC2016),* East Lansing, MI, USA, pp. THPLR003, 10.18429/JACoW-LINAC2016-THPLR003.

[5] A. Degiovanni *et al.*, "Comparison of the conditioning of high gradient accelerating structures," *Phys. Rev. Accel. Beams* Vol. 19, Iss. 3, pp. 032001, Mar. 2016, 10.1103/PhysRevAccelBeams.19.032001.

[6] A. Aksoy *et al.*, "Conceptual Design of a X-FEL Facility using CLIC X-band Accelerating Structure," in *Proc. of the 5th International Particle Accelerator Conference (IPAC2014),* Dresden, Germany, 2014, pp. THPRO025, 10.18429/JACoW-IPAC2014-THPRO025.

[7] W. Wuensch *et al.*, "R&D of X-band Accelerating Structure for Compact XFEL at SINAP," in *Proc. of the 27th Linear Accelerator Conference (LINAC2014),* Geneva, Switzerland, pp. TUPP127, 10.18429/JACoW-LINAC2016-THPLR003.

[8] M.G. Ronga *et al.*, "Back to the Future: Very High-Energy Electrons (VHEEs) and Their Potential Application in Radiation Therapy," *Cancers* Vol. 13, Iss. 19, pp. 4942, Sep. 2021, 10.3390/cancers13194942.

[9] "CLIC lights the way for FLASH therapy," CERN Courier. Geneva, Switzerland. Vol. 60, Number 6, Dec 2020. [Online] Available: https://cds.cern.ch/record/2743359. Accessed on: Dec. 12, 2022.

[10] X.-C. Li *et al.*, "Fabrication, tuning, and high-gradient testing of an X-band traveling-wave accelerating structure for VIGAS," *Nuclear Science and Techniques* Vol. 33, pp. 102, Aug. 2022, 10.1007/s41365-022-01086-y.

[11] J. Wang *et al.*, "Fabrication Technologies of the High Gradient Accelerator Structures at 100MV/m Range," in *Proc. of the 1st International Particle Accelerator Conference (IPAC'10),* Kyoto, Japan, 2010, pp. THPEA064.

[12] R. Wegner *et al.*, "Bead-Pull Measurement Method and Tuning of a Prototype CLIC Crab Cavity," in *Proc. of the 27th International Linear Accelerator Conference (LINAC2014),* Geneva, Switzerland, 2014, pp. MOPP035.

[13] U. Ellenberger *et al.*, "Status of the Manufacturing Process for the SwissFEL C-Band Accelerating Structures," in *Proc. of the 35th International Free-Electron Laser Conference (FEL2013),* New York, NY, USA, 2014, pp. TUPSO17.

[14] R. Ganter *et al.*, "SwissFEL. Conceptual Design Report," Paul Scherrer Institut (PSI), Villigen, Switzerland, Rep. No. 10-04, Jul. 2010,

[15] J.-Y. Raguin, and M. Bopp, "The Swiss FEL C-band accelerating structure: RF design and thermal analysis," in *Proc. of the 26th International Linear Accelerator Conference (LINAC2012),* Tel Aviv, Israel, 2012, pp. TUPB012.

[16] R. Zennaro *et al.*, 'Measurements and High Power Test of the First C-band Accelerating Structure for SwissFEL," in *Proc. of the 27th International Linear Accelerator Conference (LINAC2014),* Geneva, Switzerland, 2014, pp. MOPP119.

[17] T. Argyropoulos *et al.*, "Design, fabrication, and high-gradient testing of an X-band, traveling-wave accelerating structure milled from copper halves," *Phys. Rev. Accel. Beams* Vol. 21, Iss. 6, pp. 061001, Jun. 2018, 10.1103/PhysRevAccelBeams.21.061001.

[18] H. Zha, V. Dolgashev, and A. Grudiev *et al.*, "RF Design of the CLIC Structure Prototype Optimized for Manufacturing from Two Halves," in *Proc. of the 6th International Particle Accelerator Conference (IPAC2015),* Richmond, VA, USA, 2015, pp. TUPTY054.

[19] T. G. Lucas *et al.*, "Initial Testing of Techniques for Large Scale Rf Conditioning for the Compact Linear Collider," in *Proc. of the 9th International Particle Accelerator Conference (IPAC2018),* Vancouver, BC, Canada, 2018, pp. THPMK103, 10.18429/JACoW-IPAC2018-THPMK103.

[20] X. Wu *et al.*, "High Gradient Properties of a CLIC Prototype Accelerating Structure made by Tsinghua University," in *Proc. of the 7th International Particle Accelerator Conference (IPAC2016),* Busan, Korea, 2016, pp. THPOR041, 10.18429/JACoW-IPAC2016-THPOR041.

[21] X. Wu *et al.*, "High-gradient breakdown studies of an X -band Compact Linear Collider prototype structure," *Phys. Rev. Accel. Beams* Vol. 20, Iss. 5, pp. 052001, May 2017, 10.1103/PhysRevAccelBeams.20.052001.

[22] R. Zennaro *et al.*, "High Power Tests of a Prototype X-Band Accelerating Structure for CLIC," in *Proc. of the 8th International Particle Accelerator Conference (IPAC2017),* Copenhagen, Denmark, 2017, pp. THPIK097, 10.18429/JACoW- IPAC2017-THPIK097.

[23] T.G. Lucas, "High Field Phenomenology in Linear Accelerators for the Compact Linear Collider," Ph.D. dissertation, School of Physics, University of Melbourne, Melbourne, Australia, 2018.

[24] I. Syratchev, "Mode Launcher as an Alternative Approach to the Cavity-Based RF Coupler of Periodic Structures," CERN, Geneva, Switzerland, Tech. Rep. CERN-PS-RF-NOTE-2002-013, Jan. 2002.

[25] A. Grudiev, S. Calatroni, and W. Wuensch, "New local field quantity describing the high gradient limit of accelerating structures," *Phys. Rev. Accel. Beams* Vol. 12, Iss. 10, pp. 102001, Oct. 2009, 10.1103/PhysRevSTAB.12.102001.

[26] https://www.vdletg.com/en. Accessed on: Dec. 12, 2022.

[27] R. Zennaro, "Robotic disk stacking for the production of RF structures," presented at the *TESLA Technology Collaboration (TTC2020),* Geneva, Switzerland, Feb. 4–7, 2020.

[28] J. Shi, A. Grudiev, and W. Wuensch, "Tuning of X-band traveling-wave accelerating structures," *Nucl. Instrum. Meth. A* Vol. 704, pp. 14–18, Dec. 2012, 10.1016/j.nima.2012.11.182.

[29] M.S. Zarnik, and D. Belavic, "An Experimental and Numerical Study of the Humidity Effect on the Stability of a Capacitive Ceramic Pressure Sensor," *Radioengineering* Vol. 21, No. 1, pp. 201–206, Apr. 2012.

[30] B.J. Woolley, "High Power X-band RF Test Stand Development and High Power Testing of the CLIC Crab Cavity," Ph.D. dissertation, Department of Engineering, University of Lancaster, Lancaster, UK, 2015.

[31] N. Catalán Lasheras *et al.*, "Commissioning of XBox-3: A very high capacity X-band test stand," in *Proc. of the 28th Linear Accelerator Conference (LINAC2016),* East Lansing, MI, USA, pp. TUPLR047, 10.18429/JACoW-LINAC2016-TUPLR047.

[32] M. Volpi *et al.*, "High Power and High Repetition Rate X-band Power Source Using Multiple Klystrons," in *Proc. of the 9th International Particle Accelerator Conference (IPAC2018),* Vancouver, BC, Canada, 2018, pp. THPMK104, 10.18429/JACoW-IPAC2018-THPMK104.

[33] A. Balkcum *et al.*, "Industrialization effort of the SLAC XL5 klystron," in *Proc. of the IEEE International Vacuum Electronics Conference (IVEC 2012),* Monterey, CA, USA, 2012, pp. 55—56, 10.1109/IVEC.2012.6262071.

[34] F. Peauger *et al.*, "A 12 GHZ RF Power source for the CLIC study," in *Proc. of the 1st International Particle Accelerator Conference (IPAC'10),* Kyoto, Japan, 2010, pp. THPEB053.

[35] D. Sprehn *et al.*, "A 12 GHz 50MW Klystron for Support of Accelerator Research*," in *Proc. of the 1st International Particle Accelerator Conference (IPAC'10),* Kyoto, Japan, 2010, pp. THPEB065.

[36] https://etd.canon/en/index.html. Accessed on: Dec. 12, 2022.

[37] Y. Okubo, and T. Tanaka, "Development of an X-band 6 MW pulsed klystron," in *Proc. of the 11th Annual Meeting of Particle Accelerator Society of Japan,* Aomori, Japan, 2014, pp. PASJ2014-SUP049.

[38] T. Anno, Y. Okubo, and T. Tanaka, "Development of the X-band 6 MW pulsed klystron," in *Proc. of the 12th Annual Meeting of Particle Accelerator Society of Japan,* Tsuruga, Japan, 2015, pp. PASJ2015 THP062.

[39] Z.D. Farkas *et al.*, "SLED: A Method of Doubling SLAC's Energy," in *Proc. of the 9th International Conference on the High-Energy Accelerators (HEACC 1974),* Stanford, California, USA, 1974, pp. 576–583.

[40] B. Woolley, I. Syratchev, and A. Dexter, "Control and

performance improvements of a pulse compressor in use for testing accelerating structures at high power," *Phys. Rev. Accel. Beams* Vol. 20, Iss. 10, pp. 101001, Oct. 2017, 10.1103/PhysRevAccelBeams.20.101001.

[41] R. Rajamäki, "Vacuum arc localization in CLIC prototype radio frequency accelerating structures," M.S. thesis, School of Electrical Engineering, Aalto University, Espoo, Finland, 2016.

[42] J. Giner Navarro, "Breakdown studies for high gradient RF warm technology in: CLIC and hadron therapy linacs," Ph.D. dissertation, Department of Atomic, Molecular and Nuclear Physics, University of Valencia, Valencia, Spain, 2016.

[43] T.G. Lucas *et al.*, "High power testing of a prototype clic structure: Td26cc r05 n3," CERN, Geneva, Switzerland, Tech. Rep. CERN-ACC-2018-0030, Sep. 2018.

[44] A. Palaia *et al.*, "Diagnostics of RF Breakdowns in High-Gradient Accelerating Structures," in *Proc. of the 10th European Workshop on Beam Diagnostics and Instrumentation for Particle Accelerators (DIPAC2011),* Hamburg, Germany, 2011, pp. TUPD93.

[45] V. Dolgashev, "Study of Basic Breakdown Phenomena in High Gradient Vacuum Structures," presented at the *15th Linear Accelerator Conference (LINAC2010),* Tsukuba, Japan, Sep. 12–17, 2010.

[46] B. Woolley *et al.*, "High-gradient behavior of a dipole-mode rf structure," *Phys. Rev. Accel. Beams* Vol. 23, Iss. 12, pp. 122002, Dec 2020, 10.1103/PhysRevAccelBeams.23.122002.

[47] J. Paszkiewicz, "Studies of Breakdown and Pre-Breakdown Phenomena in High Gradient Accelerating Structures," Ph.D. dissertation, Department of Physics, University of Oxford, Oxford, UK, 2020. pp. 37—44.

[48] A.D. Yeremian, V.A. Dolgashev, and S.G. Tantawi, "High power S-band window optimized to minimize electric and magnetic field on the surface," in *Proc. of the IEEE International Vacuum Electronics Conference (IVEC 2014),* Monterey, CA, USA, 2014, pp. 459–460, 10.1109/IVEC.2014.6857688.

[49] A. Barnyakov *et al.*, "A High-Power S-Band RF Window for a Klystron," *Instruments and Experimental Techniques* Vol. 61, pp. 233-–238, Apr. 2018, 10.1134/S0020441218020112.

[50] Y.Joo *et al.*, "Development of new S-band RF window for stable high-power operation in linear accelerator RF system," *Nucl. Instrum. Meth. A* Vol. 866, pp. 1–8, Sep. 2017, 10.1016/j.nima.2017.05.031.

[51] W. R. Fowkes, R. S. Callin, and M. Studzinski, "Component development for X-band above 100-MW," in *Conference Record of the 1991 IEEE Particle Accelerator Conference,* San Francisco, CA, USA, 1991, pp. 713—715, 10.1109/PAC.1991.164416.

[52] W. Wuensch *et al.*, "Statistics of vacuum breakdown in the high-gradient and low-rate regime," *Phys. Rev. Accel. Beams* Vol. 20, Iss. 1, pp. 011007, Jan 2017, 10.1103/PhysRevAccelBeams.20.011007.

[53] J. Paszkiewicz, P.N. Burrows, and W. Wuensch, "Spatially resolved dark current in high gradient travelling wave structures," in *Proc. of the 10th International Particle Accelerator Conference (IPAC2019),* Melbourne, Australia, 2019, pp. WEPRB062, 10.18429/JACoW-IPAC2019-WEPRB062.

[54] E.I. Simakov, V.A. Dolgashev, and S.G. Tantawi, "Advances in high gradient normal conducting accelerator structures," *Nucl. Instrum. Meth. A* Vol. 907, pp. 221–230, Nov. 2018, 10.1016/j.nima.2018.02.085.

[55] S. Döbert *et al.*, "High Gradient Performance of NLC/GLC X-Band Accelerating Structures," in *Proc. of the 21st IEEE Particle Accelerator Conference,* Knoxville, TN, USA, 2005, pp. 372—374, 10.1109/PAC.2005.1590438.

[56] P. Burrows, W. Wuensch, and T. Argyropoulos, "High-gradient X-band RF technology for CLIC and beyond," in *Proc. of the 38th International Conference on High Energy Physics (ICHEP 2016),* Chicago, IL, USA, 2017, 10.22323/1.282.0829.

[57] J. Shi *et al.*, "Tuning of Clic accelerating structure prototypes at CERN," in *Proc. of the 25th Linear Accelerator Conference (LINAC2010),* Tsukuba, Japan, 2010, pp. MOP022.

[58] X.F.D. Stragier, P.H.A. Mutsaers and O.J. Luiten, "Smart*Light: A Tabletop, High Brilliance, Monochromatic and Tunable Hard X-ray Source for Imaging and Analysis," *Microscopy and Microanalysis* Vol. 24(S2), pp. 310–311, Aug. 2018, 10.1017/S1431927618013880.

[59] G. D'Auria *et al.*, "CompactLight DESIGN STUDY," in *Proc. of the 10th International Particle Accelerator Conference (IPAC2019),* Melbourne, Australia, 2019, pp. TUPRB032, 10.18429/JACoW-IPAC2019-TUPRB032.

[60] E. Schüler *et al.*, "Very high-energy electron (VHEE) beams in radiation therapy; Treatment plan comparison between VHEE, VMAT, and PPBS," *Medical Physics* Vol. 44, Iss. 6, pp. 2544-–2555, Jun. 2017, 10.1002/mp.12233.

[61] R. Corsini *et al.* "Status of VHEE Radiotherapy Related Studies at the CLEAR User Facility at CERN," in *Proc. of the 12th International Particle Accelerator Conference (IPAC 2021),* Campinas, SP, Brazil, 2021, pp. WEPAB044, 10.18429/JACoW-IPAC2021-WEPAB044.

[62] K.L. Tsai *et al.* "The Pulsed Magnet and Power Supply System for 50–250 MEV Electron Radiotherapy," in *2018 IEEE International Conference on Plasma Science (ICOPS),* Denver, CO, USA, 2018, p. 1, 10.1109/ICOPS35962.2018.9575460.